



Unveiling the Initiation Route of Coronal Mass Ejections through Their Slow Rise Phase

Chen Xing^{1,2} , Guillaume Aulanier^{2,3} , Xin Cheng¹ , Chun Xia⁴ , and Mingde Ding¹ ¹ School of Astronomy and Space Science, Nanjing University, Nanjing, People's Republic of China; chenxing@nju.edu.cn, xincheng@nju.edu.cn² Sorbonne Université, Observatoire de Paris-PSL, École Polytechnique, IP Paris, CNRS, Laboratoire de Physique des Plasmas, Paris, France; guillaume.aulanier@lpp.polytechnique.fr³ Rosseland Centre for Solar Physics (RoCS), Institute of Theoretical Astrophysics, Universitetet i Oslo, Oslo, Norway⁴ School of Physics and Astronomy, Yunnan University, Kunming, People's Republic of China

Received 2023 November 18; revised 2024 February 19; accepted 2024 February 23; published 2024 April 25

Abstract

Understanding the early evolution of coronal mass ejections (CMEs), in particular their initiation, is the key to forecasting solar eruptions and induced disastrous space weather. Although many initiation mechanisms have been proposed, a full understanding of CME initiation, which is identified as a slow rise of CME progenitors in kinematics before impulsive acceleration, remains elusive. Here, with a state-of-the-art thermal magnetohydrodynamics simulation, we determine a complete CME initiation route in which multiple mainstream mechanisms occur in sequence yet are tightly coupled. The slow rise is first triggered and driven by the developing hyperbolic flux tube (HFT) reconnection. Subsequently, the slow rise continues as driven by the coupling of the HFT reconnection and the early development of torus instability. The end of the slow rise, i.e., the onset of the impulsive acceleration, is induced by the start of the fast magnetic reconnection coupled with the torus instability. These results unveil that CME initiation is a complicated process involving multiple physical mechanisms, thus being hardly resolved by a single initiation mechanism.

Unified Astronomy Thesaurus concepts: Solar coronal mass ejections (310); Solar flares (1496); Solar magnetic reconnection (1504)

Supporting material: animation

1. Introduction

The Sun frequently produces violent plasma eruptions such as coronal mass ejections (CMEs), which are released into the interplanetary space and induce geomagnetic storms (Gosling 1993) and damage aerospace equipment, satellite communications, and power grids (Elovaara 2007) when colliding with the Earth's magnetosphere. The forecast of CMEs is thus extremely important for preventing space disasters and exploring habitable exoplanets (Khodachenko et al. 2007).

The evolution characteristics of CMEs and their pre-eruptive structures (e.g., sigmoids and filaments (Cheng et al. 2017); hereafter referred to as CME progenitors (Chen 2011) in kinematics at various stages lay the foundation for CME predictions. For hours to days before the eruption, CME progenitors are stable and evolve quasi-statically, rising with a small velocity ($<1 \text{ km s}^{-1}$) and tiny acceleration (Xing et al. 2018). In contrast, during the fast eruption, CMEs show an impulsive increase in velocity (up to hundreds to thousands of km s^{-1}) and acceleration (up to hundreds of m s^{-2}) in a short time (tens to hundreds of minutes; Zhang & Dere 2006). These two stages of kinematics are referred to as the quasi-static phase and the impulsive acceleration phase, respectively (Zhang et al. 2001; Zhang & Dere 2006; Xing et al. 2018). The understanding of the kinematics during these two phases is relatively thorough, where the former is believed to be a response to the photospheric motion considering their similar characteristic speeds (Yang et al. 2004; Kaithakal & Solanki 2019), and the latter is driven by the coupling of magnetohydrodynamics (MHD) instabilities

(Kliem & Török 2006; Aulanier 2014; Green et al. 2018; Aulanier 2021) and fast magnetic reconnection (Lin & Forbes 2000; Zhang & Dere 2006; Jiang et al. 2021).

The initiation of CMEs refers to the transition between the quasi-static state of CME progenitors and the impulsively eruptive state of CMEs. In theoretical works, it usually corresponds to a turning point at the start of the impulsive acceleration phase on the premise that the evolution of CME progenitors and CMEs is composed of the two phases mentioned above. Such a CME initiation is mainly explained by three mainstream mechanisms which are able to break the stable equilibria of CME progenitors (that is, to trigger the CME eruption; Aulanier 2014, 2021), i.e., (1) the torus instability (Kliem & Török 2006; Zuccarello et al. 2015) which refers to a pre-eruptive flux rope losing its equilibrium when the background constraint field decreases rapidly enough with increasing altitude, (2) the breakout reconnection (Antiochos et al. 1999; Masson et al. 2019) in which the external reconnection at a null point above the pre-eruptive structure removes the constraint of the overlying field, and (3) the tether-cutting reconnection (Moore et al. 2001; Jiang et al. 2021) in which the CME is caused by the fast reconnection with outflow jets.

However, some observational works demonstrate that CME progenitors actually always leave their quasi-static phase and experience a slow rise phase in a few to tens of minutes prior to the impulsive acceleration phase (Kahler et al. 1988; Zhang et al. 2001; Cheng et al. 2020; Prasad et al. 2023), specifically, manifesting as slowly rising with an increasing velocity (tens of km s^{-1}) and a moderate acceleration (tens of m s^{-2}) in this period (Cheng et al. 2020). Meanwhile, there is always a weak, soft X-ray enhancement as the precursor of the main flare (Simnett & Harrison 1985; Zhang et al. 2001), and the CME progenitors



Original content from this work may be used under the terms of the [Creative Commons Attribution 4.0 licence](https://creativecommons.org/licenses/by/4.0/). Any further distribution of this work must maintain attribution to the author(s) and the title of the work, journal citation and DOI.

often appear as high-temperature structures (known as hot channels) in extreme ultraviolet (EUV) bands (Cheng et al. 2012; Zhang et al. 2012). These observations indicate that the CME initiation, as the transition between the quasi-static state of CME progenitors and the impulsively eruptive state of CMEs, is actually a process before the impulsive acceleration phase, in which various precursors, including the slow rise, occur.

Different conjectures have been proposed in observations to understand the CME initiation as a process. On the one hand, it is argued that the eruption-trigger mechanism (e.g., torus instability, breakout reconnection, and tether-cutting reconnection) occurs at the start of the initiation process and drives the slow rise during the initiation (Zhang et al. 2001; Zhang & Dere 2006), considering the necessary early development of the eruption-trigger mechanism before inducing significant acceleration of CMEs (e.g., Schrijver et al. 2008). On the other hand, it is suggested that the CME initiation is related to the weak magnetic reconnection prior to the onset of eruption-trigger mechanisms, as the magnetic reconnection builds up the CME progenitor and reduces the overlying field restraining it (Sterling et al. 2007; Savcheva et al. 2012; Cheng et al. 2020; also see the review by Green et al. 2018). Specifically, Cheng et al. (2023) showed that the slow rise and the heating of CME progenitors are caused by a moderate precursor reconnection above the top of preflare loops. However, it is obvious that these two types of interpretations are disjointed, indicating that the initiation of a CME event is likely more complex than those described in the above-mentioned conjectures, and thus any single mechanism may only reveal a part of the nature of the CME initiation. To determine a complete understanding of the CME initiation and to reveal how different physics are coupled with each other, we here perform a state-of-the-art 3D observationally inspired thermal MHD simulation. The comprehensive analyses disclose a complete CME initiation that involves multiple physical mechanisms and even a coupling between two mechanisms.

2. 3D Observationally Inspired Thermal MHD Simulation of CME

2.1. Equations

In this work, we study the CME initiation by performing a 3D observationally inspired thermal MHD simulation labeled as “Simulation Driven-eruption” (abbreviated as “Simulation De”) with the code MPI-AMRVAC (Xia et al. 2018), which solves the following equations in Cartesian coordinates:

$$\frac{\partial \rho}{\partial t} + \nabla \cdot (\rho \mathbf{v}) = 0 \quad (1)$$

$$\begin{aligned} \frac{\partial (\rho \mathbf{v})}{\partial t} + \nabla \cdot \left[\rho \mathbf{v} \mathbf{v} + \left(p + \frac{B^2}{2\mu_0} \right) \mathbf{I} - \frac{B\mathbf{B}}{\mu_0} \right] \\ = \rho \mathbf{g} + 2\mu \nabla \cdot \left[\mathbf{S} - \frac{1}{3}(\nabla \cdot \mathbf{v}) \mathbf{I} \right] \end{aligned} \quad (2)$$

$$\frac{\partial \mathbf{B}}{\partial t} + \nabla \cdot (\mathbf{v} \mathbf{B} - \mathbf{B} \mathbf{v} + \psi \mathbf{I}) = -\nabla \times (\eta \mathbf{J}) \quad (3)$$

$$\begin{aligned} \frac{\partial e_{\text{int}}}{\partial t} + \nabla \cdot (e_{\text{int}} \mathbf{v}) = -p \nabla \cdot \mathbf{v} \\ + 2\mu \left[\mathbf{S} : \mathbf{S} - \frac{1}{3}(\nabla \cdot \mathbf{v})^2 \right] + \eta \mathbf{J}^2 + \nabla \cdot [\kappa_{\parallel} (\mathbf{b} \cdot \nabla T) \mathbf{b}] \end{aligned} \quad (4)$$

$$\nabla \times \mathbf{B} = \mu_0 \mathbf{J} \quad (5)$$

$$\frac{\partial \psi}{\partial t} + c_h^2 \nabla \cdot \mathbf{B} = -\frac{c_h^2}{c_p^2} \psi, \quad (6)$$

where ρ , p , T , e_{int} , \mathbf{v} , \mathbf{B} , \mathbf{J} represent the mass density, thermal pressure, temperature, internal energy, velocity, magnetic field and current density, respectively. $\mathbf{g} = -g\mathbf{e}_z$ is the gravity acceleration. μ is the dynamic viscosity coefficient and is set to 10^{-4} (in dimensionless unit) throughout the simulation, \mathbf{S} is the strain tensor where $S_{ij} = (1/2)(\partial_i v_j + \partial_j v_i)$, and \mathbf{I} is the unit tensor. η is the resistivity coefficient whose value is set differently in different phases. $\kappa_{\parallel} = 8 \times 10^{-7} T^{5/2} \text{ erg cm}^{-1} \text{ s}^{-1} \text{ K}^{-1}$ is the parallel conductivity coefficient, and $\mathbf{b} = \mathbf{B}/B$ is the normalized magnetic field. We introduce a generalized Lagrange multiplier ψ to maintain the $\nabla \cdot \mathbf{B} = 0$ condition (i.e., generalized Lagrange multiplier (GLM) method; Dedner et al. 2002). The evolution of ψ follows Equation (6), and c_h and c_p are constants. As a thermal MHD simulation, we consider compression heating, viscous dissipation, ohmic dissipation, and thermal conduction in the energy equation. In particular, we solve the internal energy equation instead of the total energy equation to avoid the heating from the numerical resistivity and numerical viscosity.

2.2. Numerical Methods

The equations are solved with the HLL scheme (Harten et al. 1983), the third-step Runge–Kutta time discretization method, and the fifth-order mp5-limited reconstruction (Suresh & Huynh 1997). We also use the magnetic field splitting method (Tanaka 1994; Xia et al. 2018) in this simulation: the magnetic field \mathbf{B} is split into two parts, the invariable background field \mathbf{B}_0 and the deviation \mathbf{B}_1 . In this simulation, \mathbf{B}_0 is set as the initial magnetic field, and thus the initial \mathbf{B}_1 is 0. This method is conducive to eliminating numerical errors related to the divergence of the magnetic field and achieving more precise results, especially in regions where the magnetic field evolves with minor change from the initial value, although it is relatively less effective in regions where the change of magnetic field is considerable (e.g., the centers of polarities during the converging phase).

The equations are solved in the dimensionless form, with the magnetic permeability equal to 1. The atmosphere is set to a fully ionized ideal gas with a hydrogen-helium abundance ratio of 10:1 (Xia et al. 2012). The dimensionless unit of the length, time, mass density, thermal pressure, temperature, velocity, and magnetic field strength is 10 Mm, 67.89 s, $2.34 \times 10^{-15} \text{ g cm}^{-3}$, 0.51 erg cm^{-3} , 1.6 MK, 147.30 km s^{-1} , and 2.53 G, respectively.

The physical domain of the simulation is in the range of $-7 \leq x \leq 7$, $-7 \leq y \leq 7$, and $0 \leq z \leq 14$ (in dimensionless unit). We set a stretched grid ($n_x \times n_y \times n_z = 144 \times 144 \times 96$), which is symmetrically stretched in x - and y -directions with a stretched ratio of 1.029, and unidirectionally stretched in z -direction with a stretched ratio of 1.028. The spatial resolution in three directions is in the range of $0.0297 \leq dx \leq 0.2262$, $0.0297 \leq dy \leq 0.2262$, and $0.0298 \leq dz \leq 0.4103$ (in dimensionless unit). In dimensional units, the finest resolutions in three directions are about 300 km, comparable to those of Solar Dynamics Observatory/Atmospheric Imaging Assembly (AIA; Lemen et al. 2012). This spatial resolution is lower than those in other simulations of CME eruptions (Aulanier et al. 2010;

Jiang et al. 2021), but it is a compromise for the sake of saving computation resources for solving the thermal MHD equations.

2.3. Initial Conditions

The initial magnetic field (similar to that in Observationally driven High-order Magnetohydrodynamics code; OHM; Aulanier et al. 2010) is composed of two potential bipolar fields:

$$\begin{aligned} B_x(t=0) &= \sum_{m=1}^4 c_m (x - x_m) r_m^{-3} \\ B_y(t=0) &= \sum_{m=1}^4 c_m (y - y_m) r_m^{-3} \\ B_z(t=0) &= \sum_{m=1}^4 c_m (z - z_m) r_m^{-3} \\ r_m &= \sqrt{(x - x_m)^2 + (y - y_m)^2 + (z - z_m)^2}, \end{aligned} \quad (7)$$

where $(c_1 = 60, x_1 = 0.9, y_1 = 0.3, z_1 = -1.1)$, $(c_2 = -60, x_2 = -0.9, y_2 = -0.3, z_2 = -1.1)$, $(c_3 = 45, x_3 = 9, y_3 = 3, z_3 = -11)$, and $(c_4 = -45, x_4 = -9, y_4 = -3, z_4 = -11)$ in dimensionless unit. The first (last) two monopoles are close to (far from) each other and located shallow (deep), producing a strong (weak) potential field that decays rapidly (slowly) with altitude within the physical domain. The first potential field mimics the background field in an active region, while the second one mimics the background field of the Sun on a global scale. The second potential field is set to ensure that the Alfvén speed at the upper part of the domain is large enough and thus to avoid shocks caused by the driving motion. The maximum dimensionless field strength in the plane $z = 0$ (which is named as box bottom surface in the following) is about 45. Such a strength is smaller than that in active regions in observations, while this is also a compromise for saving computation resources.

The initial atmosphere is set to a hydrostatic corona with a uniform dimensionless temperature of 1. The box bottom surface corresponds to 3 Mm above the solar surface, and the initial dimensionless mass density at the box bottom surface is set to 1. The initial distribution of thermal pressure and mass density with altitude follows:

$$\begin{aligned} \nabla p &= \rho g \\ p &= \rho T \\ g &= g_0 \frac{R^2}{(R + 0.3 + z)^2}, \end{aligned} \quad (8)$$

where $R_{\text{Sun}} = 69.55$ is the dimensionless solar radius and $g_0 = -0.126$ is the dimensionless gravity acceleration at the solar surface. With such an initial atmosphere, the plasma β along the vertical slit through the origin is less than 1 in the region $z < 3.7$ (in dimensionless unit) at $t = 0$. While, as the magnetic field evolves, the plasma β further decreases: the plasma β along the vertical slit through the origin is less than 1 in the region $z < 4.8$ at $t = 18$, in the region $z < 6.0$ at $t = 58$, and in the region $z < 7.5$ at $t = 68$, which ensures that the modeled CME (progenitor) is always located in a low plasma β region which mimics the corona.

The initial velocity is set to zero, and the parameter ψ is also set to zero in the whole physical domain.

2.4. Driving Motions and Line-tied Conditions

In this work, we impose line-tied motions on the bottom boundary to drive the magnetic field and set special bottom boundary conditions to ensure the line-tied condition. Here, the line-tied condition means that the footpoint of the field line can only move horizontally according to the prescribed motion in the case of ideal MHD (Aulanier et al. 2005).

Inspired by the characteristics of the photospheric magnetic field evolution in observations (Yang et al. 2004; Green & Kliem 2009; Schrijver et al. 2011), two driving motions are considered in this simulation: a shearing motion that drives the initial potential field to a highly sheared state, and a converging motion that facilitates the flux cancellation near the polarity inversion line (PIL). The “Simulation De” is composed of two phases: the shearing phase ($0 \leq t \leq 18$) with only shearing motion applied and the converging phase ($18 < t \leq 68$) with only converging motion applied. Such a setup differs from that in the previous work (Zuccarello et al. 2015), as here the converging motion is never switched off. We note that imposing only one type of motion at each phase makes the simulation easier to control and analyze. The shearing phase can be understood as a preparatory stage of the simulation to create a sheared magnetic field for the converging phase, during the latter of which we analyze the formation and eruption of the flux rope. The converging phase is designed to fulfill the flux cancellation model.

The motions are imposed at the cell-center bottom surface, which is a horizontal surface at the altitude of the cell center of the first layer of the physical domain (cell layers in the physical domain indexed by $k = 1, 2, 3, \dots, 96$ from the bottom to the top) at each time step to directly control the evolution of the magnetic field in the layer $k = 1$. For “Simulation De,” we set: the shearing motion (v_x^s, v_y^s, v_z^s):

$$\begin{aligned} v_x^s(k=1; t) &= \gamma(t) V_x^s(t) \\ v_y^s(k=1; t) &= \gamma(t) V_y^s(t) \\ v_z^s(k=1; t) &= 0 \\ V_x^s(t) &= v_0^{\max} \Psi_0(t) \partial_y \Psi(t) \\ V_y^s(t) &= -v_0^{\max} \Psi_0(t) \partial_x \Psi(t) \\ \gamma(t) &= \begin{cases} \frac{1}{2} \tanh[3.75(t-1)] + \frac{1}{2} & 0 \leq t < 16 \\ -\frac{1}{2} \tanh[3.75(t-17)] + \frac{1}{2} & 16 \leq t \leq 18 \end{cases} \end{aligned} \quad (9)$$

and the converging motion (v_x^c, v_y^c, v_z^c):

$$\begin{aligned} v_x^c(k=1; t) &= \gamma(t) V_x^c(t) \\ v_y^c(k=1; t) &= \gamma(t) V_y^c(t) \\ v_z^c(k=1; t) &= 0 \\ V_x^c(t) &= v_0^{\max} \Psi_0(t) \partial_x \Psi(t) \\ V_y^c(t) &= v_0^{\max} \Psi_0(t) \partial_y \Psi(t) \\ \gamma(t) &= \frac{1}{2} \tanh[3.75(t-19)] + \frac{1}{2} \quad 18 < t \leq 68, \end{aligned} \quad (10)$$

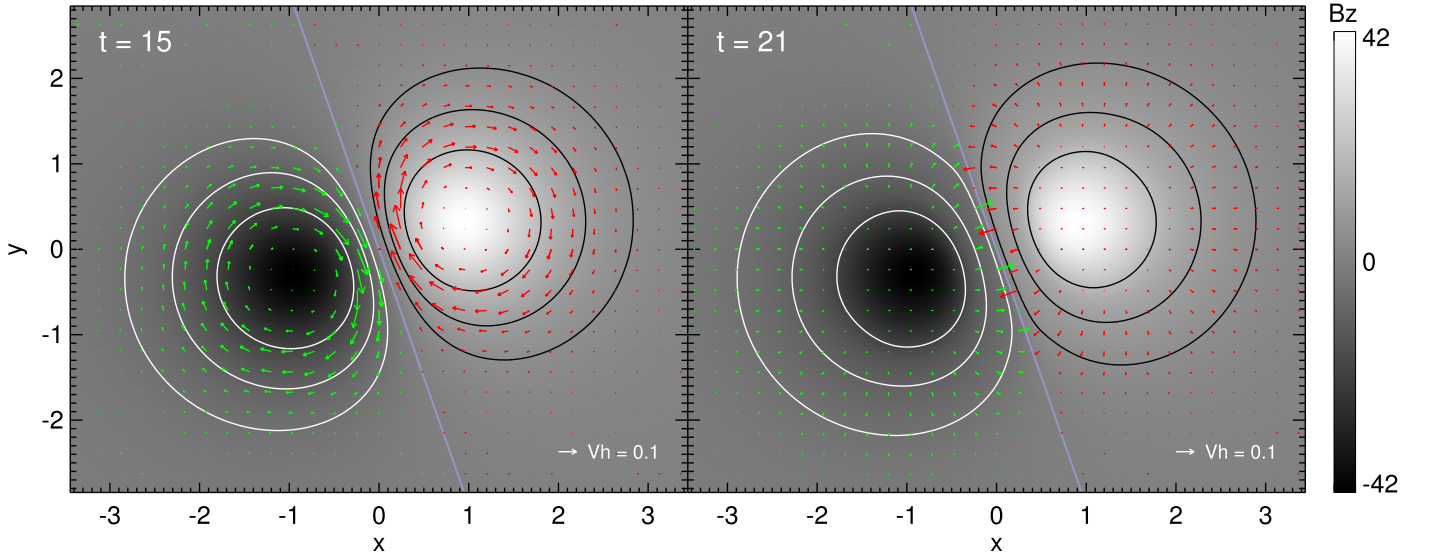


Figure 1. Distribution of B_z and imposed horizontal driving motions on the cell-center bottom surface. The black (white) contours in the positive (negative) polarity are the contours of B_z , and the purple ones show the PILs. The red (green) arrows in the positive (negative) polarity in the left panel show the shearing flow at $t = 15$, and those in the right panel show the converging flow at $t = 21$. The arrow orientation denotes the direction of the motion, and its length represents the magnitude of the speed (v_h). The scale of v_h is shown at the bottom right corner of each panel. All parameters are in dimensionless units.

where

$$\Psi(t) = \exp \left[-\Psi_1 \left(\frac{B_z(k=1; t)}{B_z^{\max}(k=1; t)} \right)^2 \right], \quad (11)$$

and $\Psi_1 = 5.5$ for the shearing motion and $\Psi_1 = 27.5$ for the converging motion. The maximum speed of the driving motion v_0^{\max} is set to 0.16 (in dimensionless unit) for both the shearing and the converging motions. The function $\Psi_0(t)$ is used to keep the maximum of the term $\sqrt{V_x^2 + V_y^2}$ always v_0^{\max} . As shown in Figure 1, the shearing motion is along the tangent direction of the contour of $B_z(k=1)$, while the converging motion is perpendicular to that tangent direction. Near the PIL, the shearing motion is antiparallel on two sides of the PIL, while the converging motion is toward the PIL.

It should be noted that the maximum speed of the driving motions is set to roughly 20 times that in observations to speed up the simulation. While, it is still acceptable as it is less than the Alfvén speed and the sound speed in the core area affected by the driving motion: at $t=0$, in the domain that $-4.20 \leq x \leq 4.20$, $-4.20 \leq y \leq 4.20$, and $0 \leq z \leq 8.36$ (in dimensionless unit), the ratio of v_0^{\max} to the average Alfvén speed is 0.101 and the ratio of v_0^{\max} to the maximum Alfvén speed is 0.004; the ratio of v_0^{\max} to the sound speed is constant of 0.124 in this domain.

Several settings are adopted to achieve the line-tied condition at the cell-center bottom surface. First, the GLM parameter ψ is fixed to zero in the layer $k=1$, and we set a symmetric boundary condition centered at the cell-center bottom surface for ψ (see Section 2.5 for more details), so all components of the term $\nabla \cdot (\psi \mathbf{I})$ are zero in the layer $k=1$. Second, for “Simulation De,” in the layer $k=1$, the dissipation

term in Equation (3) is modified into:

$$\begin{aligned} & \frac{\partial \mathbf{B}}{\partial t} + \nabla \cdot (\mathbf{v} \mathbf{B} - \mathbf{B} \mathbf{v} + \psi \mathbf{I}) \\ &= \begin{cases} 0 & 0 \leq t \leq 18 \\ \eta \left(\frac{\partial^2}{\partial x^2} + \frac{\partial^2}{\partial y^2} \right) \mathbf{B} & 18 < t \leq 68. \end{cases} \end{aligned} \quad (12)$$

During the shearing phase of “Simulation De” ($0 \leq t \leq 18$), the dissipation term in this layer equals zero so that it has no effect on the magnetic field. The resistivity η is fixed to zero in the layer $k=1$ and set to be uniform ($\eta = 10^{-4}$; in dimensionless unit) in the whole region (including both the physical domain and the ghost cell layers) except the layer $k=1$ during the shearing phase. However, during the converging phase of “Simulation De” ($18 < t \leq 68$), we adopt a 2D dissipation term (Aulanier et al. 2010) in the layer $k=1$ to allow the flux cancellation close to the PIL. A larger, uniform resistivity ($\eta = 4 \times 10^{-4}$; in dimensionless unit), which facilitates the flux cancellation, is set in the whole region, including the layer $k=1$.

In addition, the shearing motion in Equation (9) satisfies that the z -component of the term $\nabla \cdot (\mathbf{v} \mathbf{B} - \mathbf{B} \mathbf{v})$ is zero, so analytically B_z in the cell-center bottom surface should remain invariable during the shearing phase. To achieve this feature more accurately, we enforce that B_z remains invariable in the layer $k=1$ during this phase.

2.5. Boundary Conditions

The mp5-limited reconstruction method uses three ghost cell layers at each boundary. The mesh in the ghost cell layer is also stretched in the same way as that in the physical domain. In all ghost cell layers, the background magnetic field \mathbf{B}_0 remains

invariable; the two components of the magnetic field \mathbf{B}_1 which are parallel to the boundary surface are derived by one-sided third-order equal-gradient extrapolation, and the component of \mathbf{B}_1 which is normal to the boundary surface is derived under the constraint of the $\nabla \cdot \mathbf{B} = 0$ condition. Such a setting will keep the divergence of the magnetic field zero in the layer $k = 1$, so it is reasonable to set ψ to zero in this layer.

We assume that at each time step, the atmosphere in both the bottom ghost cell layer and the layer $k = 1$ is hydrostatic. Thus, the thermal pressure in the bottom ghost cell layer can be derived with a centered difference. We further assume that the dimensionless temperature in the ghost cell layer is constant of 1, the same as the initial temperature, and then the mass density is derived by the ideal gas law. The thermal pressure and the mass density in the top ghost cell layers are derived with the same method. In the four side ghost cell layers, the thermal pressure and the mass density are fixed to their initial values.

The velocity in the bottom ghost cell layer $k = n$ (layer indexed by $k = -1, -2, -3$ from the top to the bottom of the bottom ghost cells) is derived from the velocity in the layer $k = 1$ and that in the layer $k = 1 - n$ by the linear extrapolation. This boundary condition is the same as the antisymmetric boundary condition for v_z and the pseudo antisymmetric boundary condition for v_x and v_y at the bottom boundary in the previous work (Aulanier et al. 2005). The velocity in top ghost cell layers is derived by the one-sided second-order zero-gradient extrapolation, and the z -component is forced to be no less than zero to avoid possible downward flows. The velocity in the side ghost cell layers is set by the antisymmetric boundary condition centered on the side surface of the box.

To achieve the goal of removing the contribution of $\partial_z \psi$ in the layer $k = 1$, a symmetric bottom boundary condition for ψ is set centered on the cell center of this layer. The aim is fulfilled more precisely by replicating the flux of ψ from the top surface of the layer $k = 1$ to its bottom surface (box bottom surface). In the top and the side ghost cell layers, ψ is fixed to zero.

2.6. Overview of Modeled CME Event

The evolution of the modeled CME progenitor and CME in “Simulation De” is shown in Figure 2. During the shearing phase ($0 \leq t \leq 18$), the initial potential field is driven to a highly sheared state under the shearing motion (Figure 2(b)). After that, during the converging phase ($18 < t \leq 68$), a pre-eruptive flux rope composed of twisted field lines is first formed by magnetic reconnection under the converging motion, and then it erupts as a CME (Figure 2(b)). The pre-eruptive flux rope is hot and visible in synthetic EUV images mimicking AIA 335 Å observations (Figures 2(a) and 10).

The initial magnetic topology of the reconnection region is a bald patch (BP; Titov et al. 1993; during $20 \leq t \leq 45$), characterized by $(\mathbf{B} \cdot \nabla)B_z > 0$ where $B_z = 0$. As shown by the quasi-separatrix layers (QSLs; Priest & Démoulin 1995), such a BP topology later gradually bifurcates into a hyperbolic flux tube (HFT; Titov et al. 2002; since $t = 46$; see Figures 5 and 8(f)). An obvious difference between the BP reconnection and the HFT reconnection is that the former forms flux rope field lines tangent to the bottom surface at their dips (Figure 3(a)), while the latter forms flux rope field lines whose dipped parts are detached from the bottom surface and low-lying loops (Figure 3(b)).

3. Kinematics of CME Progenitor and CME

The kinematics of the CME progenitor and CME in “Simulation De” is estimated by measuring the height of the apex of an overlying field line right above the flux rope. Such an estimation method in simulations is consistent with the estimation method in observations where the kinematics of the hot channel is measured at its leading edge. The overlying field line is selected as one traced from the same fixed point at the center of the positive polarity and on the cell-center bottom surface. The velocity at this fixed point is extremely small, very close to or equal to zero, in all phases of “Simulation De,” which ensures that the footpoint of this field line hardly moves and its height evolution can well reflect that of the CME (progenitor).

The kinematics of CME progenitor and CME, as shown in Figure 4, is composed of three phases which are comparable to the three phases in observations, even though the simulation is merely designed for CME progenitor formation and CME eruption and certainly it is not designed to fit the kinematics a priori. The CME progenitor first rises quasi-statically with a tiny and fluctuating acceleration (during $35 \leq t < 52$; Figure 4(f)), consistent with the behavior in the quasi-static phase in observations (Xing et al. 2018). As a result, the velocity-time curve is in a quasi-linear form in this phase (Figure 4(e)). We note that the decaying fluctuation of the acceleration may reflect the process of the CME progenitor gradually approaching the quasi-equilibrium state under the driving motion. Later (during $52 \leq t \leq 65$), the acceleration of the flux rope continuously increases to tens of m s^{-2} (Figure 4(f)), and thus its velocity increases quickly (Figure 4(e)). This phase corresponds to the slow rise phase in observations and thus marks the initiation process of the modeled CME, as this phase is just before the impulsive acceleration of the CME, and the evolution of acceleration in it is significantly different from those in phases both before and after it. Even the acceleration in this phase is comparable to that in the slow rise phase in observations (also tens of m s^{-2} ; Cheng et al. 2020). The last phase ($65 < t \leq 68$) is considered to correspond to the impulsive acceleration phase in observations, as the modeled CME acceleration impulsively rises to hundreds of m s^{-2} in this period (Figure 4(c)).

The eruption of CME is most likely triggered by torus instability (TI), which occurs in the later stage of the slow rise phase (at a moment during $59 \leq t < 63$; see the analysis of torus instability in Appendix A). Other potential eruption-trigger mechanisms are ruled out: (1) The HFT reconnection can not trigger the eruption as the flux rope fails to erupt in the presence of the HFT in the control simulation “Simulation Ne” (see Appendix A). (2) The long and thin current sheet, which is usually necessary for fast magnetic reconnection (Jiang et al. 2021), does not show up before $t = 65$ in this simulation. Therefore, the fast magnetic reconnection, even if it sets in this simulation, occurs later than the onset of the torus instability and does not play a key role in triggering the eruption.

Lastly, it should be noted that the behavior of the acceleration of the CME progenitor is less affected by the absolute speed of the driving motion during the quasi-static phase in this simulation. The reason is that the rising of the CME progenitor is a response to the driving motion in this phase, while the maximum speed of driving motions is a

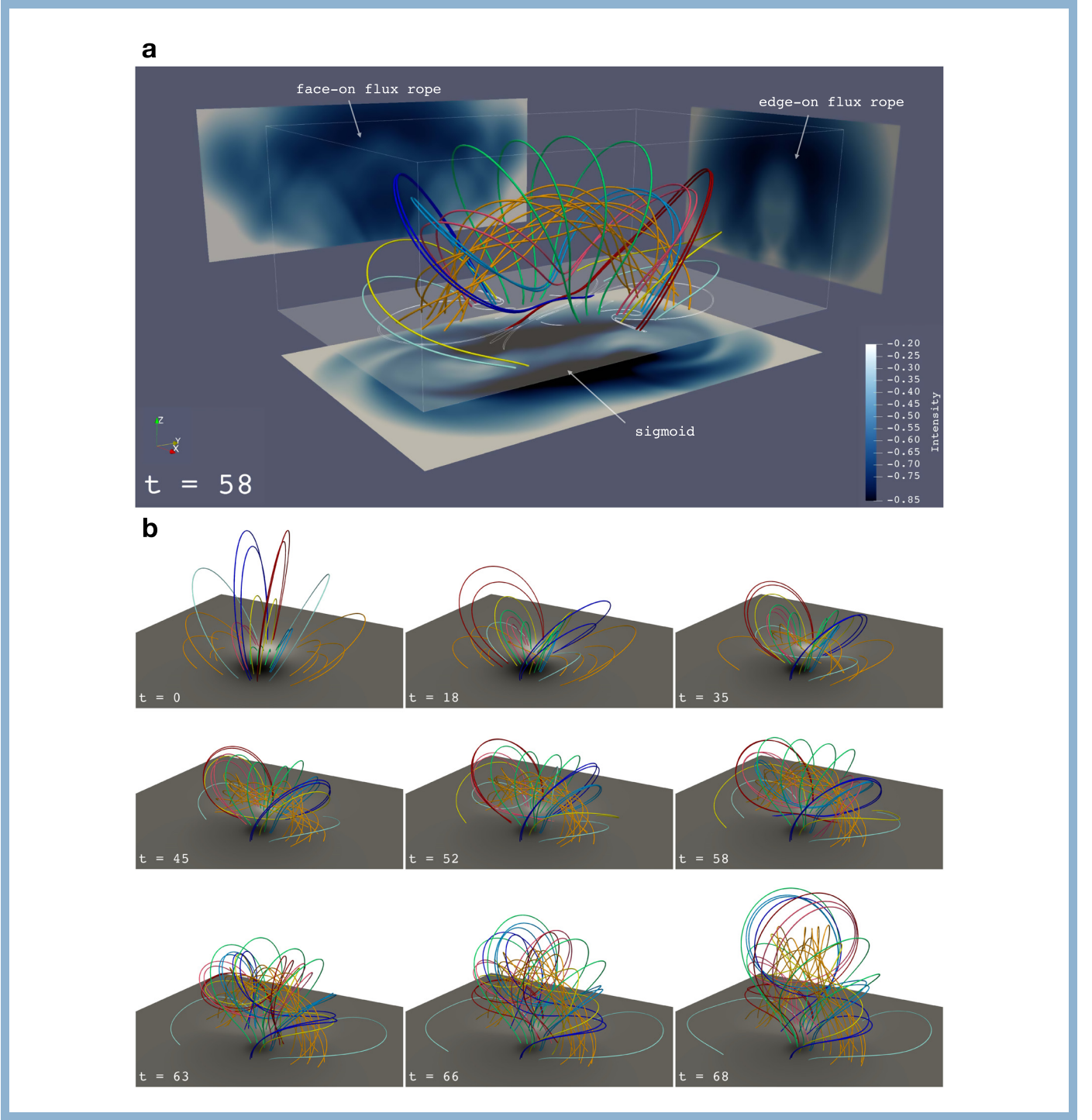


Figure 2. Overview of the formation and eruption of the modeled flux rope. (a) Field lines and percentage difference of synthetic EUV images at the AIA 335 Å at $t = 58$. The left, right, and bottom images are the synthetic images observed from x -, y -, and z -directions, respectively. The translucent surface corresponds to the cell-center bottom surface and the box is used for integrating the emissivity. The white contours on the bottom surface represent those of QSL footprints. The three side views of this panel are shown in Figure 10(c). (b) Evolution of magnetic field lines. The subpanel at $t = 58$ is the same as panel (a). The cyan field line at $t = 35$ and the yellow field line at $t = 45$ are tangent to the bottom surface at their dips, representing the field lines traced from the bald patch. The light blue and light red field lines at $t = 52$ and the dark blue and dark red field lines at $t = 58$ exhibit those passing through the hyperbolic flux tube. The cell-center bottom surface shows the distribution of B_z . White (black) represents the positive (negative) polarity. The scale of B_z is the same in each subpanel. An animation of panel (b) is available, showing the evolution of field lines from $t = 0$ to $t = 68$ in the simulation. The duration of the animation is 23 s.

(An animation of this figure is available.)

constant. Therefore, even if the absolute speed of the driving motion is large, the acceleration of the CME progenitor, as the first-order derivative of the velocity with

respect to time, is still almost close to 0. Therefore, the quasi-static phase in our simulation can be compared to that in observations.

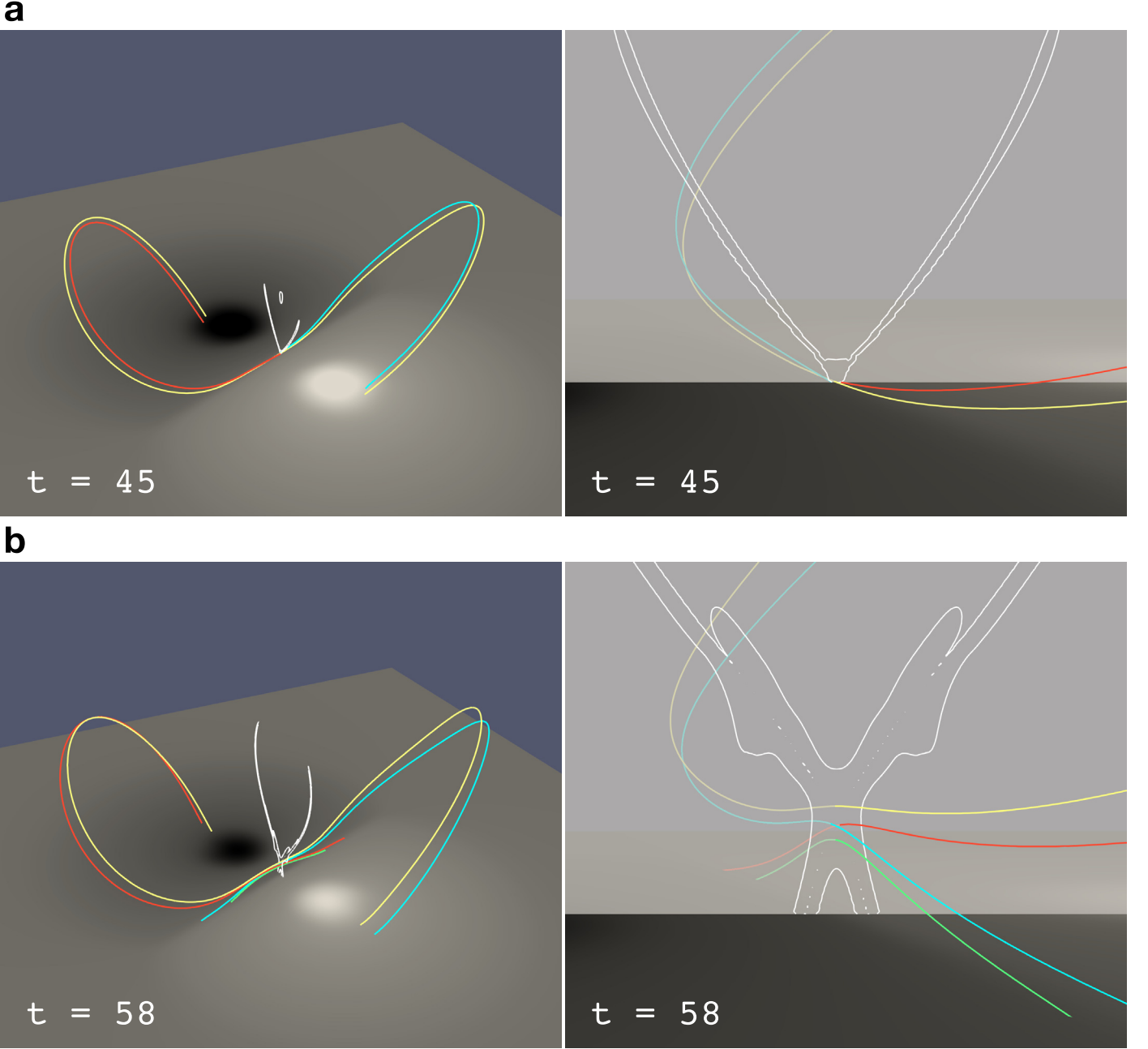


Figure 3. Sketches of reconnections. (a) A sketch of the bald patch (BP) reconnection. The BP reconnection occurs between two sheared arcades (symbolized by the red and the blue field lines) at two sides of the BP and forms a flux rope field line (symbolized by the yellow field line) which is tangent to the bottom surface at its dip. The cell-center bottom surface shows the distribution of B_z . The white contours show the profiles of the QSLs in the plane $y = 0$. The white vertical plane in the right subpanel is the plane $y = 0$. (b) A sketch of the HFT reconnection. The HFT reconnection occurs between two sheared arcades (symbolized by the red and blue field lines) at the right and left sides of the HFT. It forms a flux rope field line (symbolized by the yellow field line) whose dipped part is detached from the bottom surface and at the upper part of the HFT and a low-lying loop (symbolized by the green field line) at the lower part of the HFT. The cell-center bottom surface, white contours, and the white vertical plane have the same meanings as those in panel (a).

4. Mechanisms of Kinematics

4.1. Triggering Mechanism of Slow Rise Phase

The transition from the quasi-static phase to the slow rise phase occurs (at $t = 52$) just after the first appearance of HFT (at $t = 46$). This indicates that the HFT reconnection is likely the mechanism triggering the slow rise phase.

This speculation is supported by detailed analyses of the relation between the reconnection and the kinematics. Figures 5(a), (f) reveal that the upward outflow of the

reconnection is very slow at the stage of BP (e.g., $t = 45$) and the early stage of HFT ($46 \leq t < 52$), but it is markedly accelerated as the HFT is rapidly built up (e.g., from $t = 52$ to $t = 58$). Quantitatively, the growth rate of the reconnection upward outflow velocity is temporally consistent with the acceleration of the CME progenitor, and both of them start to increase shortly after the first appearance of HFT (Figure 5(g)). We consider that the velocity of the reconnection upward outflow reflects the ability of reconnection to contribute to the flux rope. Therefore, the above results indicate that the slow

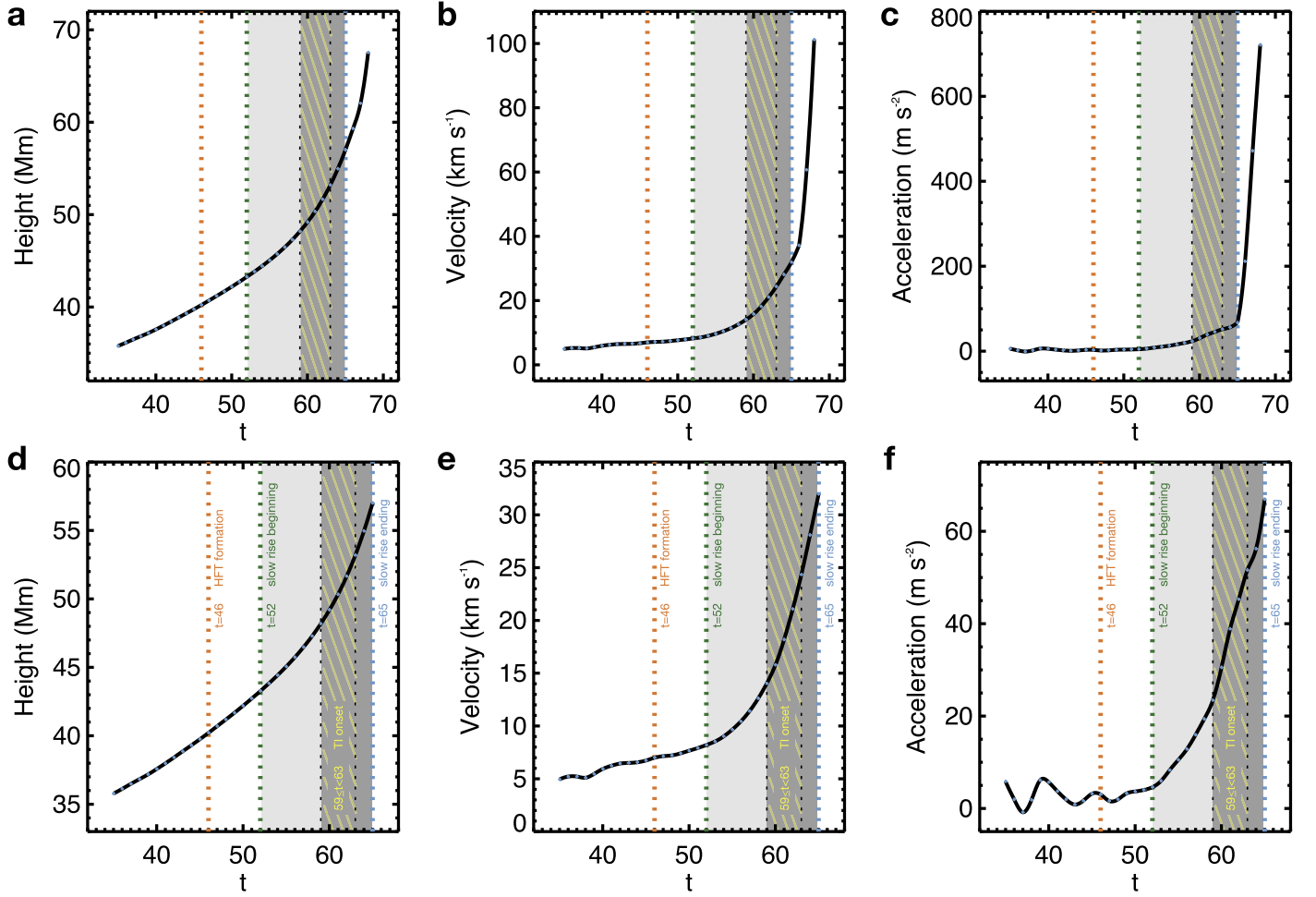


Figure 4. Kinematics of the CME progenitor and CME. (a)–(c) Kinematics of the CME progenitor and CME during $35 \leq t \leq 68$. In each panel, the blue points show the measured or derived data and the black curve shows the fitting curve of data with the cubic spline interpolation method. The orange dashed line represents the time when the HFT first appears. The green and blue dashed lines mark the beginning and the end of the slow rise phase, respectively. The light gray and dark gray regions show the earlier stage and the later stage of the slow rise phase, respectively. The two black dashed lines and the yellow oblique-line region between them mark the time range of the torus instability onset. (d)–(f) Same as panels (a)–(c) but for the kinematics during $35 \leq t \leq 65$.

rise is triggered when the contribution from reconnection starts to quickly increase after the HFT forms. In other words, the slow rise is triggered by the HFT reconnection. We eliminate the possibility that the torus instability triggers the slow rise, since the failed eruption in “Simulation Ne” implies that the torus instability, as the triggering mechanism of the eruption, does not occur before $t=58$ in the “Simulation De” (see Appendix A).

4.2. Driving Mechanisms of Slow Rise Phase

We further investigate the mechanisms driving the slow rise of the flux rope. Considering that the torus instability occurs during the slow rise phase, we divide the slow rise phase into two stages, i.e., the earlier stage ($52 \leq t \leq 58$) and the later stage ($59 \leq t \leq 65$), and analyze the driving mechanisms in these two stages separately.

For the earlier stage, the motion of the flux rope is controlled by a net upward force on its lower part and a net downward force on its upper part (see Figure 6(b), taking an example at $t=58$). The Lorentz force and the thermal pressure gradient force are the major contributors to the net force, while the gravity and the viscous force are of little importance (Figure 6). Especially, the maxima of the Lorentz force, the net force, and

the velocity in the flux rope region are all concentrated near the HFT (Figures 6(a), (b)) during this stage. This implies that it is the HFT reconnection that powers the flux rope rise in the earlier stage of the slow rise phase. In addition, the synchronized evolutions of the flux rope acceleration and the growth rate of the reconnection upward outflow velocity in Figure 5(g) also indicate that the slow rise is driven by the HFT reconnection during the earlier stage.

The HFT reconnection drives the slow rise in the earlier stage, on the one hand, by adding twisted concave-upward field lines to the lower part of the flux rope (Figure B1). These field lines provide magnetic tension to the flux rope (Figure 6(a); known as the slingshot effect), enhance the force imbalance in the flux rope, and finally accelerate the flux rope. On the other hand, the reconnection upward outflow in the HFT is convected upwardly into the flux rope (Figures 5(a), (e)), and thus it can directly promote the flux rope rise. Specifically, the plasma in the reconnection upward outflow is accelerated by a net upward force which is dominated by the Lorentz force and the thermal pressure gradient force (Figure 5). The upward Lorentz force consists of magnetic tension force mainly at the HFT top and magnetic pressure gradient force mainly at the HFT center (Figure 7), the former of which is provided by the newly formed concave-upward field lines and the latter of which is

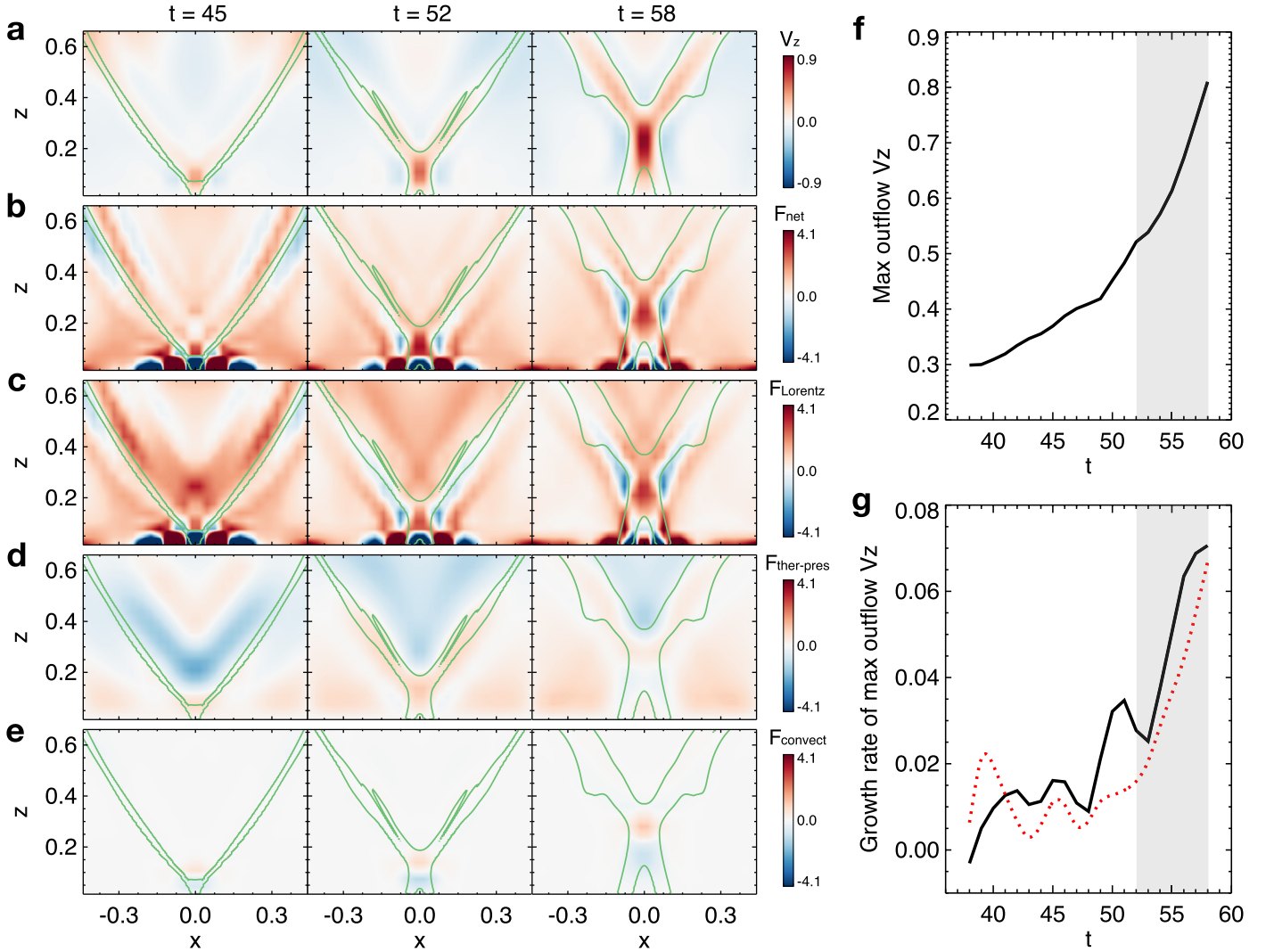


Figure 5. Evolutions of forces and velocity in the reconnection region. (a)–(e) Component of forces and velocity in the z -direction in the plane $y=0$ at $t=45$, $t=52$, and $t=58$. They are in order as follows: velocity (v_z ; panel (a)), net force (F_{net} ; panel (b)), Lorentz force (F_{Lorentz} ; panel (c)), thermal pressure gradient force ($F_{\text{ther-pres}}$; panel (d)), and force related to the convection (F_{convect} ; panel (e)). F_{net} is the sum of the z -components of Lorentz force, thermal pressure gradient force, gravity, and viscous force. All of the forces and velocities are in dimensionless units. The green contours outline the QSLs, indicating that the magnetic topology of the reconnection region is a BP at $t=45$ and an HFT at $t=52$ and $t=58$. (f) The maximum z -component of velocity (v_z ; in dimensionless unit) of the reconnection outflow along the vertical slit through the origin during $38 \leq t \leq 58$. The gray region shows the slow rise phase before $t=58$. (g) The black curve shows the growth rate of the maximum v_z of the reconnection outflow during $38 \leq t \leq 58$, which is derived by taking the derivative of the maximum v_z with respect to time. The red dashed curve represents the fitting curve of the flux rope acceleration before $t=58$, which is the same as that in Figure 4(f) but numerically scaled down by a factor of 290. The gray region has the same meaning as that in panel (f).

associated to the accumulation of the sheared/guide component of the magnetic field. The upward thermal pressure gradient force is due to an increase in the gas pressure at the flanks of the flux rope bottom, which is a result of the density pileup pinched by the reconnection inflow (Figure 7).

Furthermore, since the HFT appears, the two footprints of the HFT continuously separate from each other in the direction perpendicular to the PIL, and meanwhile they extend in the direction parallel to the PIL to both sides until they are completely separated (Figures 8(a)–(c); shown by the QSL footprint, which manifests as the flare ribbon in observations during the eruption (Zhao et al. 2016), but probably invisible before the eruption due to the weak reconnection rate). The reconnection electric field within the HFT, which represents the reconnection rate (Forbes & Priest 1984), also shows a

gradually increasing trend since $t=46$ and until $t=59$ (Figure 8(h); also see Appendix C for more details). These results strongly suggest that the HFT and its associated reconnection are gradually built up during the earlier stage of the slow rise phase. Both the slingshot effect and the outflow effect of the HFT reconnection thus become stronger, which leads to the continuous increase of acceleration of the CME progenitor in this stage.

For the later stage of the slow rise phase, we argue that the HFT reconnection still has a considerable contribution to the rising motion, since the HFT reconnection becomes even stronger in this stage, shown by the quickly increasing reconnection electric field (see that during $59 \leq t \leq 65$ in Figure 8(h)). Moreover, the torus instability also promotes the slow rise in the later stage since it starts. On the one hand, the

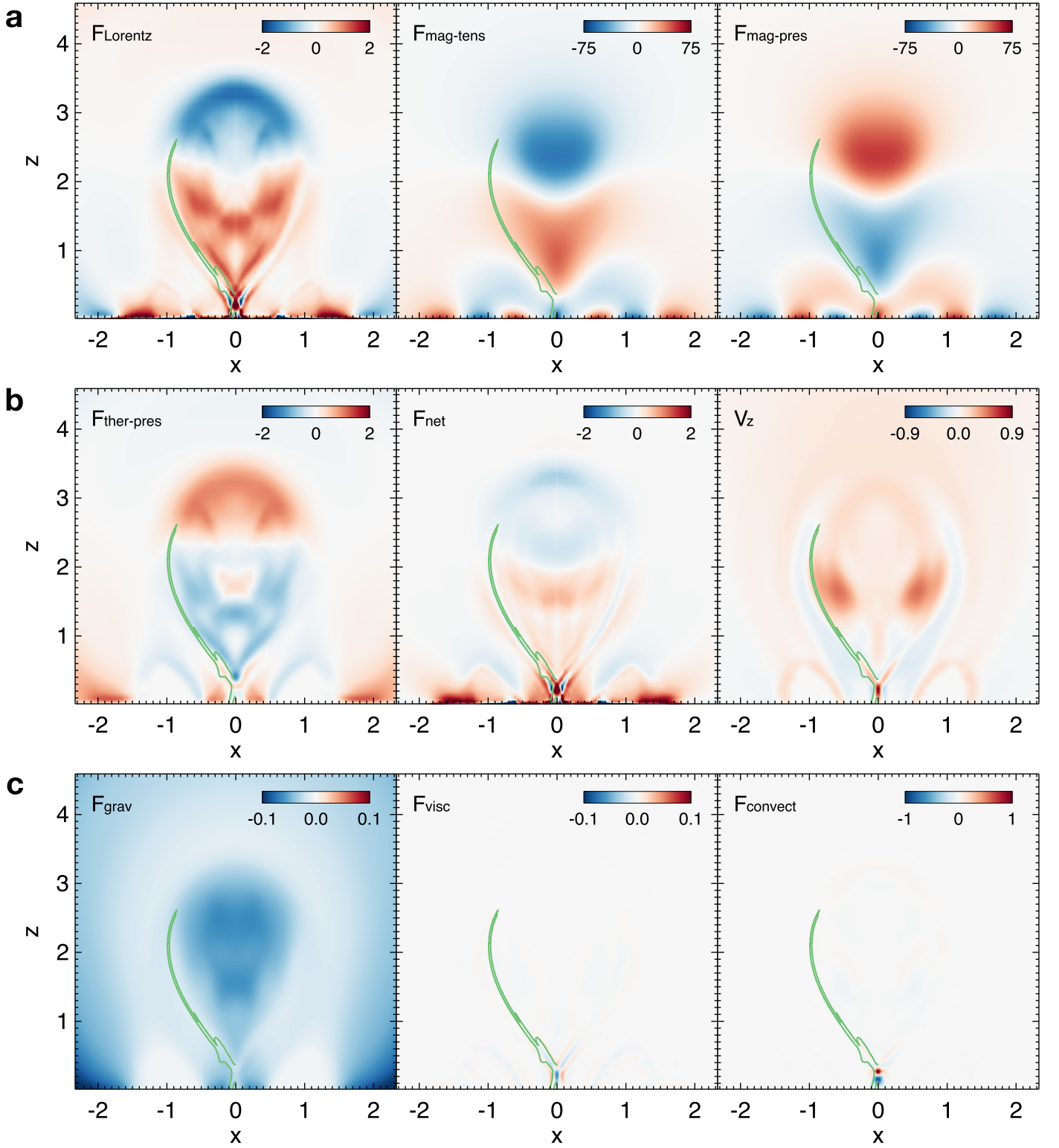


Figure 6. Component of forces and velocity in the z -direction in the plane $y = 0$ at $t = 58$. They are in order as follows: Lorentz force (F_{Lorentz}), magnetic tension force ($F_{\text{mag-tens}}$), magnetic pressure gradient force ($F_{\text{mag-pres}}$), thermal pressure gradient force ($F_{\text{ther-pres}}$), net force (F_{net}), velocity (v_z), gravity (F_{grav}), viscous force (F_{visc}), and force related to the convection (F_{convect}). F_{net} is the sum of F_{Lorentz} , $F_{\text{ther-pres}}$, F_{grav} , and F_{visc} . Here the $F_{\text{mag-tens}}$ ($F_{\text{mag-pres}}$) is derived by first decomposing $\mathbf{B} \cdot \nabla \mathbf{B}$ ($-\nabla(B^2/2)$) to the normal direction of the magnetic field and then further decomposing to the z -direction, given that the tangential component does not contribute to the acceleration. All of the forces and the velocity are in dimensionless units. The green contours represent the profiles of QSLs in the half panel of $x \leq 0$. See Appendix B for more details for locating the flux rope boundary.

hoop force could directly accelerate the flux rope (Kliem & Török 2006); on the other hand, the torus instability could indirectly contribute to the slow rise by enhancing the HFT

reconnection, evidenced by that the HFT reconnection electric field immediately shows a quick increase once the torus instability sets in (Figure 8(h)). This enhancement may be due

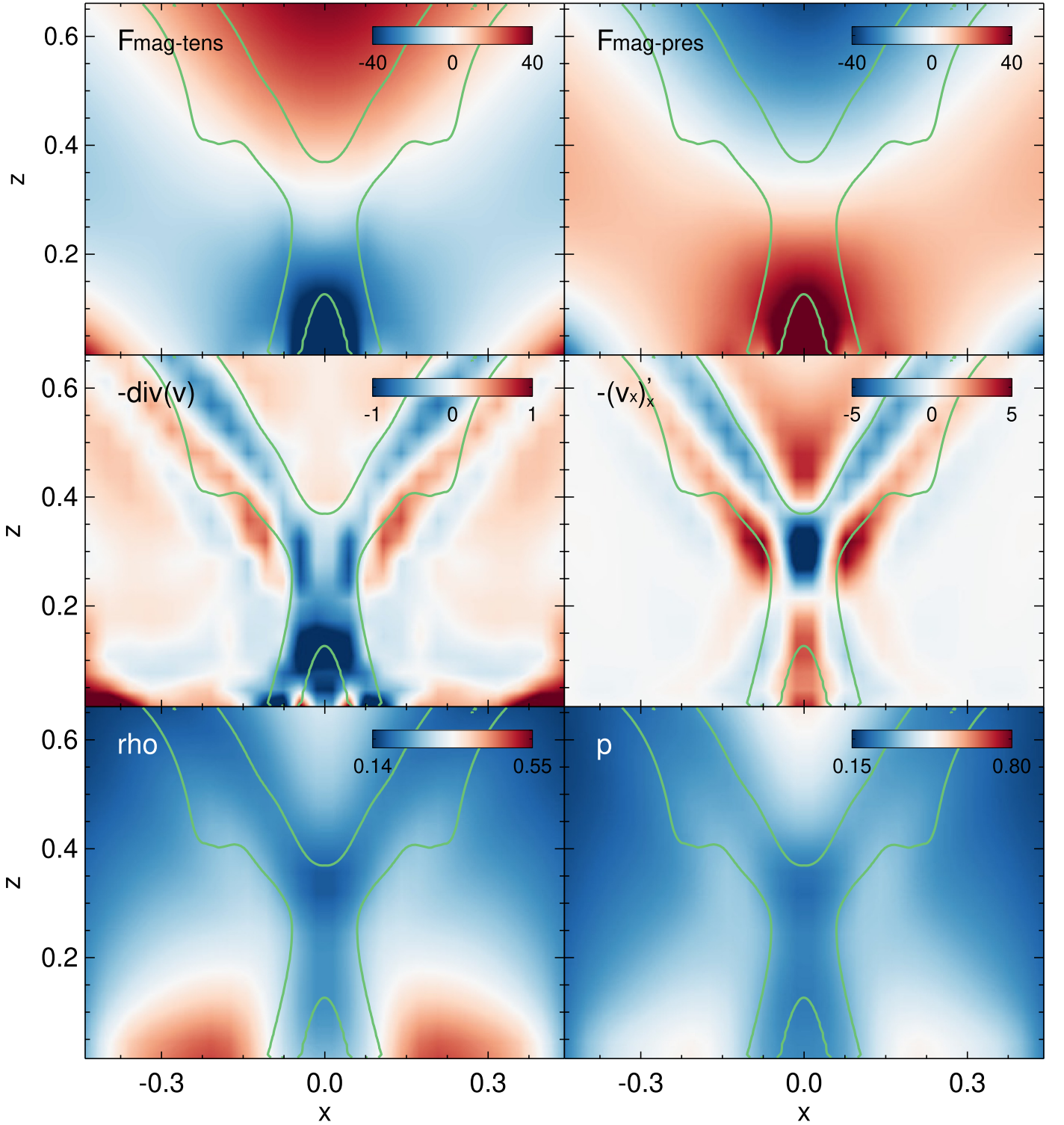


Figure 7. Some parameters related to force analysis on the plane $y=0$ at $t=58$. They are in order as follows: z-component of magnetic tension force ($F_{\text{mag-tens}}$), z-component of magnetic pressure gradient force ($F_{\text{mag-pres}}$), the negative divergence of velocity ($-\text{div}(\mathbf{v})$), the negative partial derivative of x-component of velocity to x ($-(v_x)_x$), mass density (ρ), and thermal pressure (p). All parameters are in dimensionless units. The positive $-\text{div}(\mathbf{v})$ and $-(v_x)_x$ at the two flanks of the flux rope bottom clearly show the compression caused by the reconnection inflow. The green curves represent the contours of the QSLs.

to the phenomenon that the current structure in the HFT could become longer as the flux rope rises higher and faster with the contribution from the torus instability, which well reflects the close coupling of torus instability and HFT reconnection in the later stage.

4.3. Triggering and Driving Mechanisms of Impulsive Acceleration Phase

A fast magnetic reconnection likely occurs during the impulsive acceleration phase, as a thin and long current sheet, which is usually the necessary condition for the fast magnetic

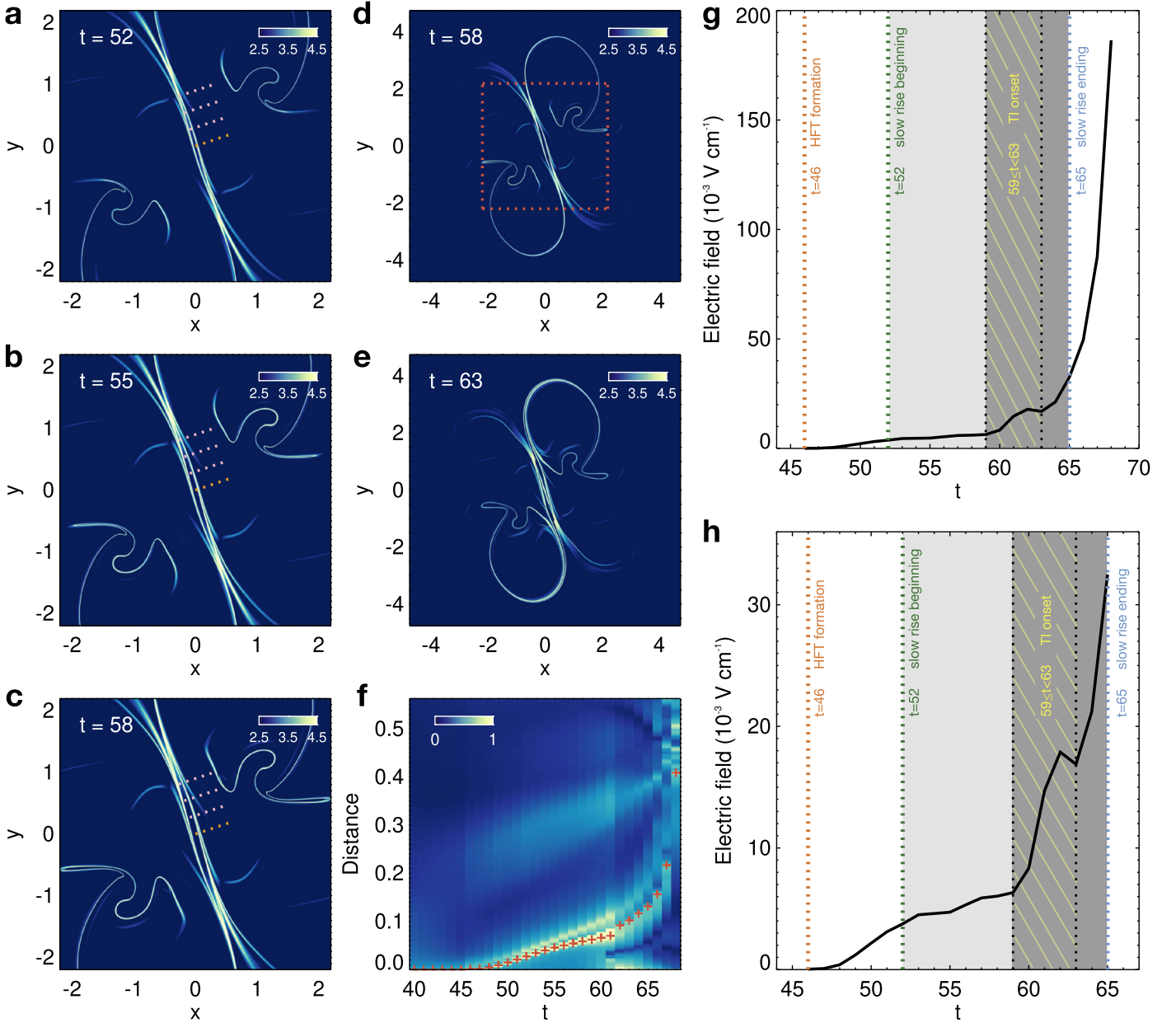


Figure 8. Evolutions of HFT footprint and HFT reconnection electric field. (a)–(c) Squashing degree $\log Q$ on the cell-center bottom surface at $t = 52$, $t = 55$, and $t = 58$. The field of view is marked by the red dashed box in panel (d). (d)–(e) Squashing degree $\log Q$ on the cell-center bottom surface at $t = 58$ and $t = 63$. The two hook-shape QSL footprints around $(X, Y) = (1, 2)$ and $(X, Y) = (-1, -2)$ mark the boundaries of two footpoints of the flux rope, respectively. At the ends of straight parts of QSL footprints (around $(X, Y) = (-2, 2)$ and $(X, Y) = (2, -2)$ in panel (e)), the curved QSL footprints demonstrate the rapid change in the connectivity of the field lines anchored there as a result of the driving motion. (f) Time-slice plot of the normalized $\log Q$. The slit is denoted by the orange dashed line in panels (a)–(c). At each moment, $\log Q$ is normalized by the maximum $\log Q$ along the slit, and the red symbol marks the location of the local maximum of normalized $\log Q$ which corresponds to the HFT footprint. (g) Reconnection electric field E during $46 \leq t \leq 68$. The reconnection electric field during $46 \leq t \leq 51$ is derived from the orange slit in panels (a)–(c); the reconnection electric field during $52 \leq t \leq 68$ is averaged from the electric fields derived from four slits (represented by the orange and the pink dashed lines in panels (a)–(c)). The vertical dashed lines, light/dark gray regions, and yellow oblique-line region have the same meanings as those in Figure 4. (h) Same as panel (g) but for the reconnection electric field E during $46 \leq t \leq 65$.

reconnection, is formed at the start of the impulsive acceleration phase ($t \sim 66$) and soon built up since then (Figure 9). The other evidence for the fast magnetic reconnection is the impulsively increasing reconnection electric field in the reconnection region during the impulsive acceleration phase (Figure 8(g)). Therefore, we consider that the impulsive acceleration phase ($65 < t \leq 68$) is likely triggered as the magnetic reconnection coupled to the torus instability transforms from the relatively weaker HFT reconnection to the relatively stronger fast magnetic reconnection, and that the

phase is continuously driven by the close coupling of the fast magnetic reconnection and the torus instability which induces an impulsive acceleration.

5. Heating of CME Progenitor

Benefitting from the thermal MHD simulation, we also study the thermal properties of the CME progenitor. The modeled CME progenitor is significantly heated and visible in EUV synthetic images at the AIA 335 Å (Figures 2(a) and 10; see

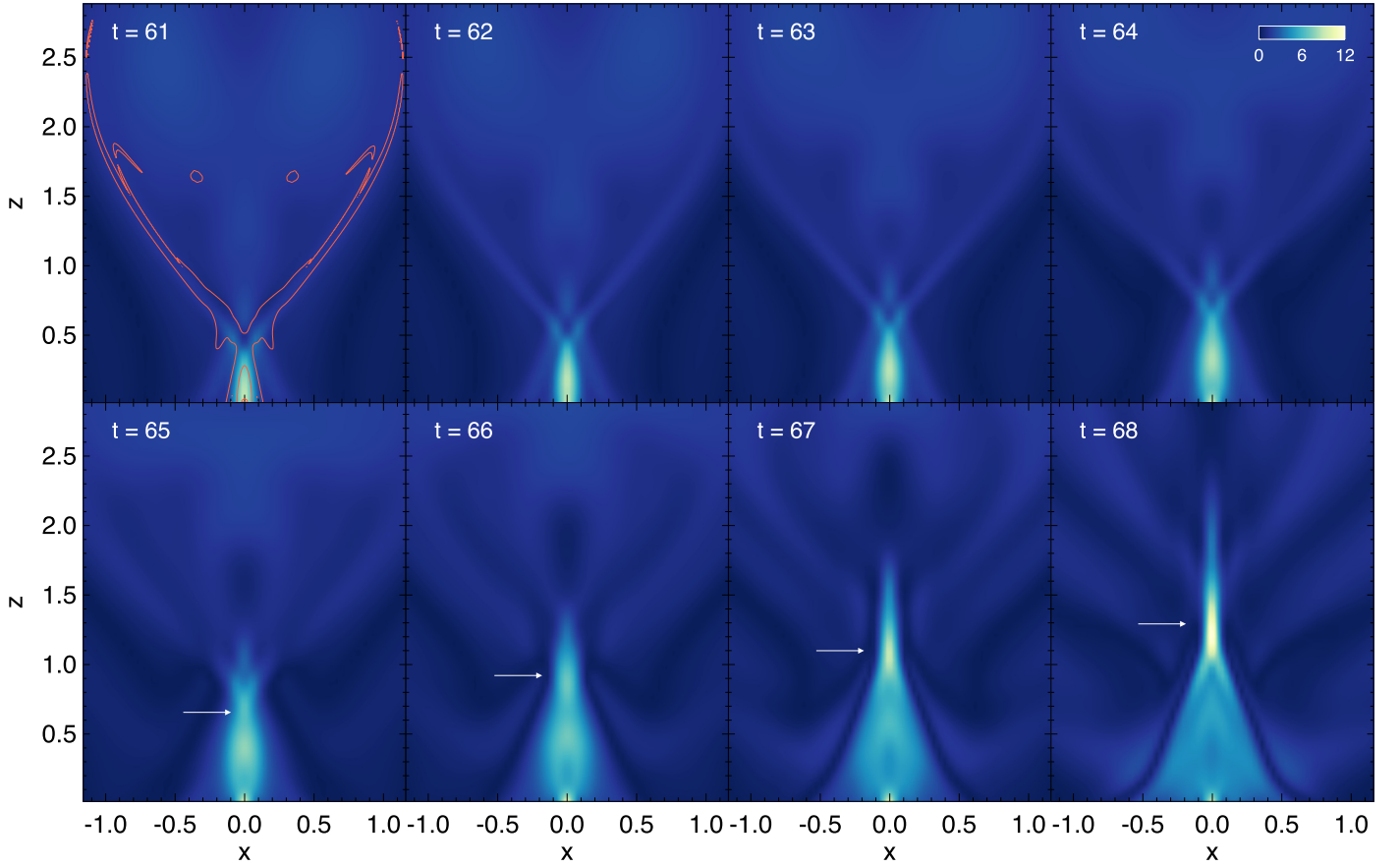


Figure 9. Current structures in the reconnection region during $61 \leq t \leq 68$. Each panel shows the distribution of dimensionless J/B on the plane $y = 0$. The color bar for J/B in all panels is displayed at the upper right corner. The red contours in the first panel show the outlines of QSLs at $t = 61$. The white arrows mark the forming current sheet in the reconnection region.

Appendix D for more details). It is channel-like in the face-on view, elliptical in the edge-on view, and sigmoidal in the top view. It is very similar to pre-eruptive hot channels discovered in observations (Zhang et al. 2012; Patsourakos et al. 2013; Cheng et al. 2014), except that our modeled one is somewhat less hot than those in observations due to the weak magnetic field adopted in our simulation. The temperature of the modeled CME progenitor is expected to increase with a stronger magnetic field, as the former is roughly proportional to the square of the latter. Regardless of the specific temperature, the modeled bright structure basically corresponds to the pre-eruptive flux rope (Figure 10), which supports the view that the hot channel represents the hot flux rope in observations (Zhang et al. 2012).

In addition, taking the snapshot at $t = 58$ as an example, an analysis of the heating sources reveals that the CME progenitor is mainly heated by the ohmic dissipation (Figure 11). Especially, one can find that at the bottom and side boundaries of the flux rope, the ohmic dissipation is relatively stronger and its profile is highly consistent with that of the HFT and the QSLs (Figure 11). This result indicates that the magnetic reconnection in the HFT and the QSLs surrounding the flux rope effectively heats the local plasma while it forms the pre-eruptive flux rope, which confirms the conjecture in the previous 3D CME model (Janvier et al. 2014). In addition, the bulk heating within the flux rope results from the setup of a uniform resistivity in the simulation domain.

6. Summary: A Complete Route of CME Initiation

Based on our simulation, we present a complete route of the CME initiation, as summarized in Figure 12. In short, during the CME initiation, the slow rise motion is first triggered and driven by the HFT reconnection and later driven by an early coupling of the HFT reconnection and the torus instability.

In detail, the kinematic evolution around the CME initiation is described as the following. With the magnetic topology of the reconnection region changing from the BP to the HFT, the HFT reconnection starts to promote the flux rope rising with its slingshot effect and reconnection upward outflow. As the HFT reconnection develops, the effect of the HFT reconnection to the flux rope rise gradually increases and eventually starts the slow rise phase/CME initiation. Afterward, at the earlier stage of the slow rise phase/CME initiation, the pre-eruptive flux rope rises slowly with an increasing acceleration owing to the progressively enhanced HFT reconnection. With the HFT-dominated slow rise going on, the flux rope later reaches a critical height where the torus instability sets in. The onset of the instability marks the onset of the CME eruption in the physical sense, i.e., the flux rope being out of equilibrium. Then, at the later stage of the slow rise phase/CME initiation, the torus instability induces a stronger HFT reconnection, and they together promote the slow rise of the flux rope. Finally, the impulsive acceleration of CME starts (the CME initiation ends) when the magnetic reconnection coupled to the torus instability transforms from the HFT reconnection to the fast magnetic

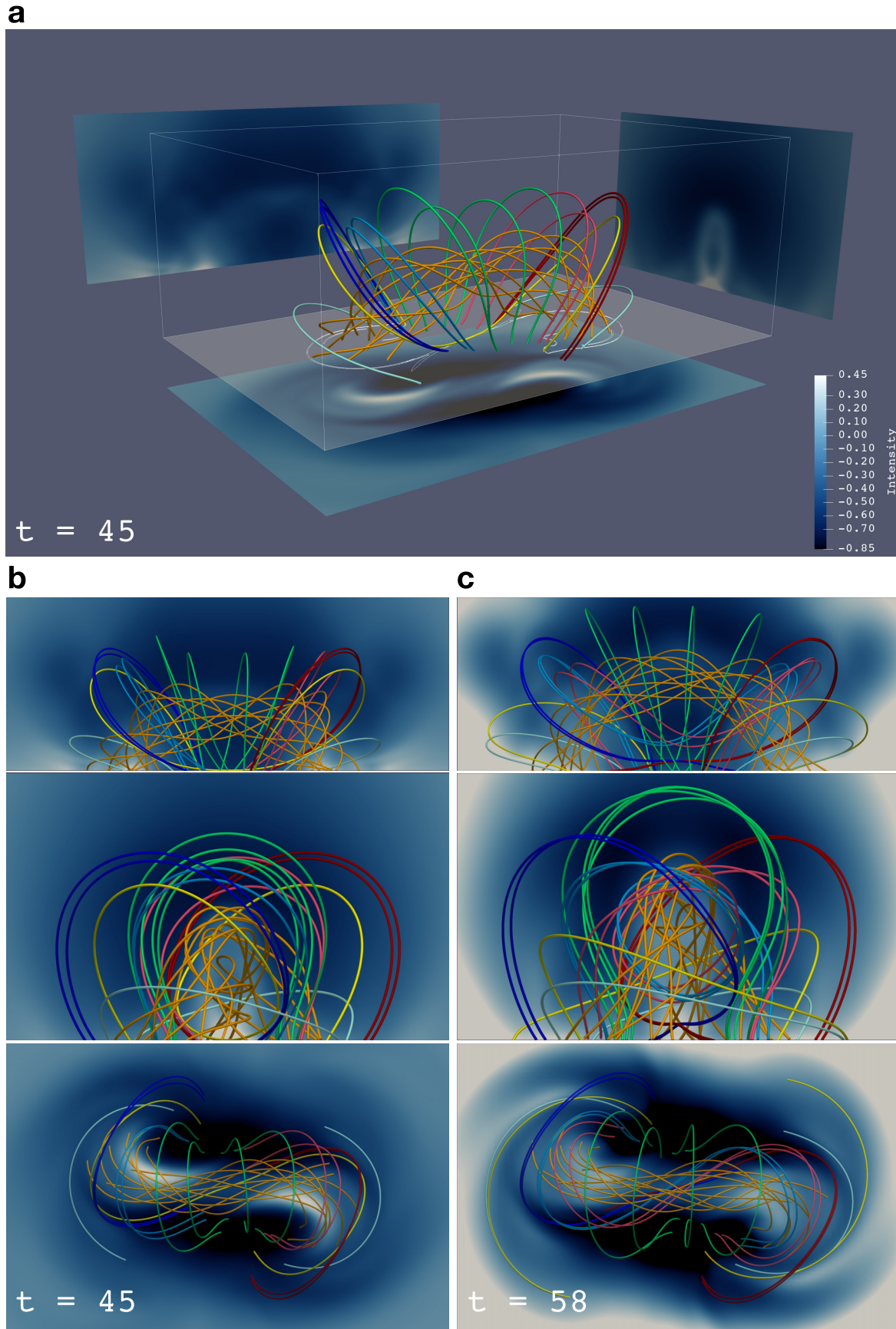


Figure 10. Magnetic field lines and synthetic EUV images at the AIA 335 Å. (a) Same as Figure 2(a) but for $t = 45$. (b) Three side views of field lines and percentage difference images at $t = 45$. (c) Same as the panel (b) but for $t = 58$.

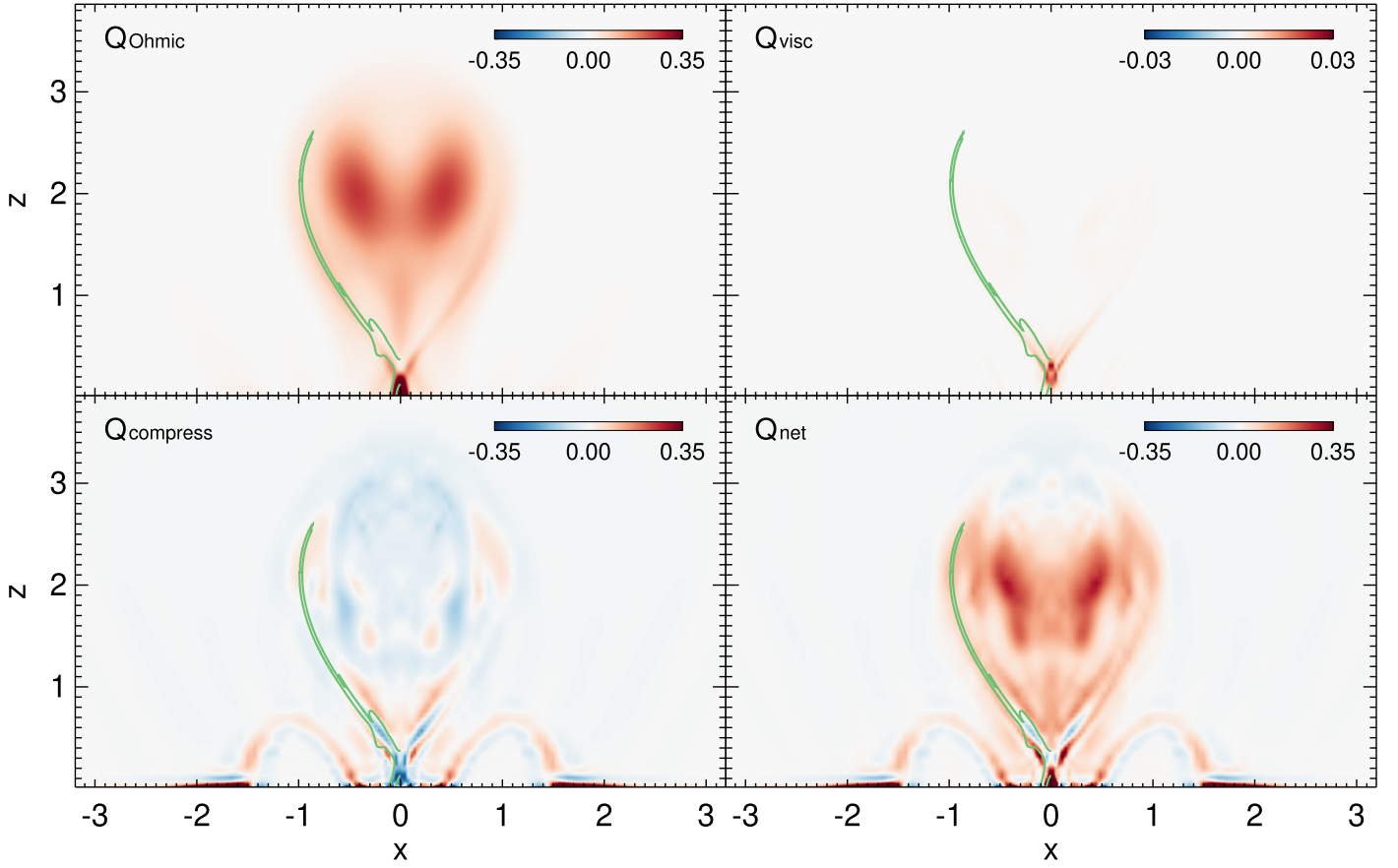


Figure 11. Heating rates on the plane $y = 0$ at $t = 58$. They are in order as follows: rates of ohmic heating (Q_{ohmic}), viscous heating (Q_{visc}), compression heating (Q_{compress}), and net heating (Q_{net}) which is the sum of the first three. All heating rates are in dimensionless units. The field of view is the same as that of the synthetic image along the y -direction in Figure 2(a). The green contours represent those of QSLs at the half panel of $x \leq 0$.

reconnection, which is later than the eruption onset in the physical sense.

7. Discussion

In previous studies, the slow rise motion during the initiation process was explained by a single mechanism, such as the eruption-trigger mechanism (Zhang et al. 2001; Zhang & Dere 2006) or the weak magnetic reconnection before the onset of eruption-trigger mechanisms (Sterling et al. 2007; Savcheva et al. 2012; Cheng et al. 2020, 2023). In contrast, our work presented here reveals that the CME initiation is actually a multiple-physics coupled process and its complete route is hardly to be explained by the previous single mechanism. First, the HFT reconnection triggers the CME initiation and drives the CME progenitor to slowly rise in quasi-equilibrium. Second, after the torus instability triggers the eruption, the less energetic destabilization and the HFT reconnection jointly contribute to the slow rise/CME initiation for a while until the coupling of the destabilization and the fast magnetic reconnection begins and induces the impulsive acceleration of the CME.

For the HFT reconnection, our simulation especially provides insight into the question of how it drives the flux rope during the initiation process. We find that both the Lorentz force and the thermal pressure gradient force play important roles in the slow rise phase, at least in its earlier stage. Quantitatively, for the flux rope field lines at the upper part of the HFT, the ratio of the maximum of the thermal pressure gradient force to that of the Lorentz force is roughly 40% at

$t = 52$ and 12% at $t = 58$ (Figures 5(c), (d); the plasma β is roughly 0.01 at regions of the above-mentioned maximum of the force). This result for the first time confirms the previous conjecture on the key role of Lorentz force in causing the rise of pre-eruptive structures in the “tether-cutting reconnection” model (Moore et al. 2001). However, the contribution of thermal pressure gradient force to the slow rise is also not negligible, while this result could be further influenced by the plasma β in the HFT reconnection region. This underscores the indispensability of a thermal MHD simulation, beyond the zero- β MHD simulations (Aulanier et al. 2010; Zuccarello et al. 2015), in the study of the CME initiation.

Another important finding in our work is that the impulsive acceleration of CMEs does not immediately start at the onset of the torus instability but commences at a later moment when the coupling of the torus instability and the fast magnetic reconnection starts. Such a time delay may explain why the critical decay indices estimated in observations (Zou et al. 2019; Cheng et al. 2020, 2023) are sometimes larger than those derived theoretically (Kliem & Török 2006; Démoulin & Aulanier 2010), as the observationally determined eruption onset time is probably later than the real onset time of the torus instability in these works. It should be mentioned that a larger magnetic field strength in observations compared to that in this simulation may lead to a larger kinematic acceleration, and thus the above-mentioned time delay may become shorter in observations. In addition, such a time delay indicates that the torus instability can only induce a relatively small acceleration

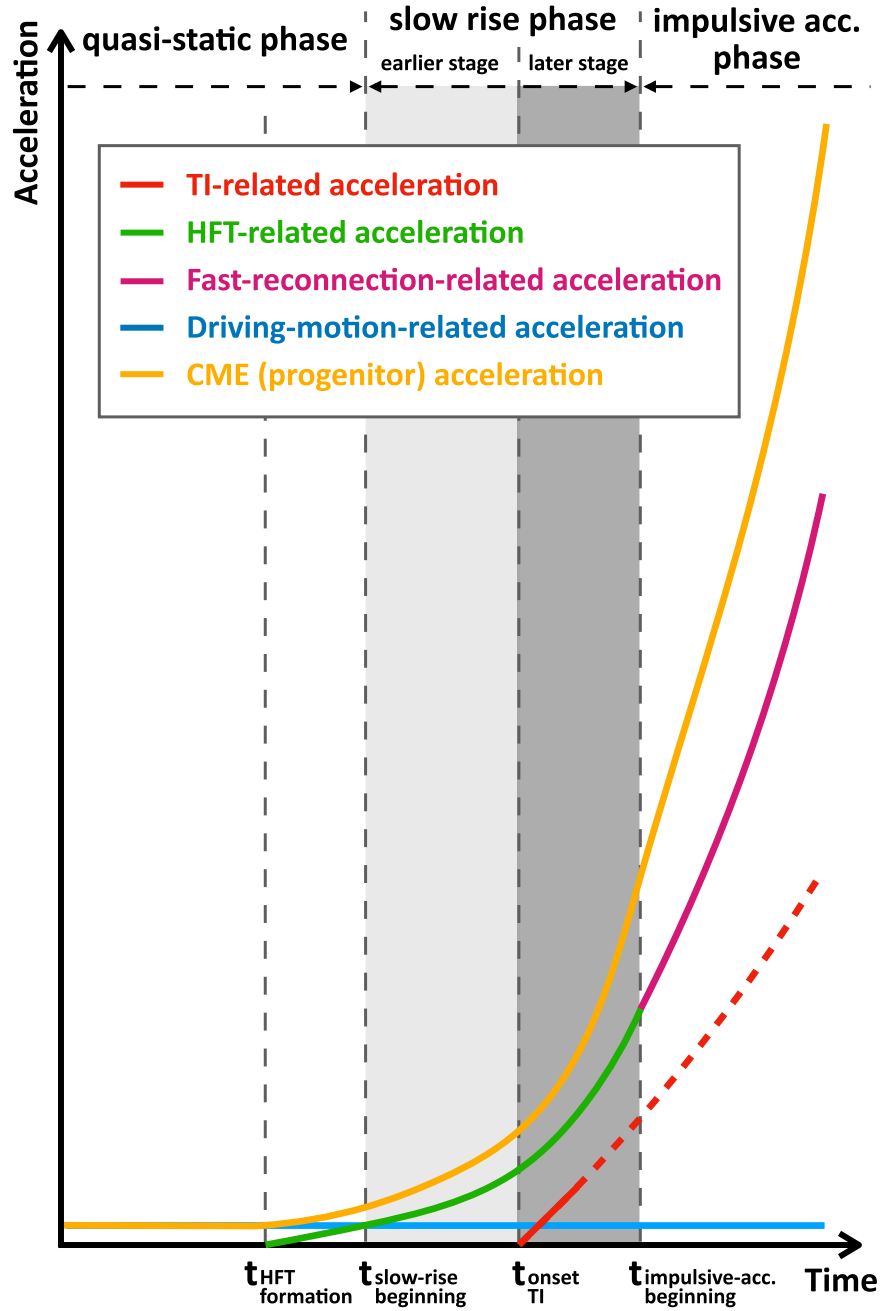


Figure 12. Physical processes as disclosed by the kinematics of the CME progenitor and CME. The yellow curve represents the acceleration of the CME (progenitor). The red, green, purple, and blue curves show the four accelerations contributed by the torus instability, the HFT reconnection, the fast magnetic reconnection, and the driving motion, respectively. The onset times of the HFT, the slow rise, the torus instability, and the impulsive acceleration (abbreviated as acc.) of the CME are displayed by four dashed lines and labeled as $t_{\text{HFT-formation}}$, $t_{\text{slow-rise-beginning}}$, $t_{\text{onset-TI}}$, and $t_{\text{impulsive-acc.-beginning}}$, respectively. In our simulation, these four onset times correspond to $t = 46$, $t = 52$, a moment during the period $59 \leq t < 63$, and $t = 65$, respectively. The light gray and dark gray regions show the earlier stage and the later stage of the slow rise phase/CME initiation process, respectively. The red curve is dashed during a part of the slow rise phase and the impulsive acceleration phase, indicating that the dominant mechanism for the acceleration is unknown whether it is torus instability or magnetic reconnection in these periods.

at its beginning compared to that in the impulsive acceleration phase. Lastly, we emphasize that the finding on the time delay benefits from the setup of our simulation, i.e., continuously imposing driving motion after the eruption is triggered. Such a setup is distinguished from that in previous works (Aulanier et al. 2010; Zuccarello et al. 2015), in the latter of which the driving motion is switched off to relax the system during the eruption. Our simulation avoids the extra relaxation effect in previous works, which does not occur in observations but could also contribute to the time delay in simulations and

pose a significant difficulty for analysis (as discussed in Appendix A.2).

Our simulation sheds light on the heating process of CME progenitors. However, it should be noted that the thermodynamics in our simulation is a simplification of that of the Sun for the sake of clear and concise results. First, the density and the temperature profiles of the atmosphere were simplified in the simulation by omitting the lower atmosphere (from the photosphere to the transition region) and setting a uniform coronal temperature. Second, some processes in flares, e.g., the

radiative cooling and the chromospheric evaporation, were not taken into account in the simulation. Even so, we emphasize that these simplifications do not critically affect our result, i.e., the magnetic reconnection takes place in the current sheet surrounding the flux rope and builds up and heats the CME progenitor.

In summary, we successfully reproduce the complete early kinematics of a CME event with a 3D thermal MHD simulation that is more physically realistic in this work. For the first time, we explicitly disentangle the complex CME initiation process by systematically investigating how various mechanisms play roles at different stages of the kinematics of a CME event.

Acknowledgments

We thank Yuhao Zhou, Jinhan Guo, Yang Guo, Rony Keppens, Can Wang, and Feng Chen for valuable discussions. C.X. and G.A. acknowledge financial support from the French National Space Agency (Centre National d'Etudes Spatiales; CNES), as well as from the Programme National Soleil Terre (PNST) of the CNRS/INSU also cofunded by the CNES and the French Alternative Energies and Atomic Energy Commission (Commissariat à l'Énergie Atomique; CEA). C.X. also acknowledges financial support from the China Scholarship Council. X.C. and M.D.D. are supported by the National Key R&D Program of China under grants 2021YFA1600504 and NSFC under grant 12127901. The numerical calculations in this paper were done on the computing facilities in the High Performance Computing Center of Nanjing University and the Cholesky computing cluster from the IDCS mesocentre at Ecole Polytechnique. MPI-AMRVAC 2.2, the code used to perform the simulation in this paper, is an open-source code. It is available from the website <https://amrvac.org/index.html>. The code used to calculate the squashing degree is available from the website <https://github.com/el2718/FastQSL>.

Appendix A

Analysis of Onset Time of Torus Instability

A.1. Control Simulations

In this work, we perform three control simulations to help us determine the onset time of the torus instability in “Simulation De.” In the following, we first introduce the numerical setups in these three control simulations.

The first control simulation, referred to as “Simulation Half-driven-eruption” (abbreviated as “Simulation He”), is composed of two phases: the shearing phase ($0 \leq t \leq 18$) and the converging phase ($18 < t \leq 70$). The setups in “Simulation He” are the same as those in “Simulation De,” except that the amplitude of the converging flow is gradually switched off to half during $59 < t \leq 60$ and then kept at half after that ($60 < t \leq 70$) by modifying the function of $\gamma(t)$ in Equation (10) in these periods:

$$\gamma(t) = \begin{cases} -\frac{1}{4} \tanh[6.0(t - 59.5)] + \frac{3}{4} & 59 < t \leq 60 \\ \frac{1}{2} & 60 < t \leq 70, \end{cases} \quad (\text{A1})$$

The second control simulation, referred to as “Simulation Undriven-eruption” (abbreviated as “Simulation Ue”), is composed of three phases: the shearing phase ($0 \leq t \leq 18$), the converging phase ($18 < t \leq 60$), and the relaxation phase ($60 < t \leq 71$). Before and at $t = 59$, the setups of “Simulation

Ue” are the same as those of “Simulation De.” After $t = 59$, the converging flow is gradually switched off to zero during $59 < t \leq 60$, and then the velocity on the cell-center bottom surface is fixed to zero during the relaxation phase ($60 < t \leq 71$), also by modifying the function of $\gamma(t)$ in Equation (10) in these periods:

$$\gamma(t) = \begin{cases} -\frac{1}{2} \tanh[6.0(t - 59.5)] + \frac{1}{2} & 59 < t \leq 60 \\ 0 & 60 < t \leq 71. \end{cases} \quad (\text{A2})$$

Correspondingly, during $59 < t \leq 71$, the dissipation term in the Equation (3) in the layer $k = 1$ is modified into:

$$\begin{aligned} & \frac{\partial \mathbf{B}}{\partial t} + \nabla \cdot (\mathbf{v} \mathbf{B} - \mathbf{B} \mathbf{v} + \psi \mathbf{I}) \\ & = \begin{cases} \eta \left(\frac{\partial^2}{\partial x^2} + \frac{\partial^2}{\partial y^2} \right) \mathbf{B} & 59 < t \leq 60 \\ 0 & 60 < t \leq 71. \end{cases} \end{aligned} \quad (\text{A3})$$

During $59 < t \leq 60$, the setup of η is the same as that during $18 < t \leq 59$. During the relaxation phase ($60 < t \leq 71$), η is set to zero in the layer $k = 1$ and set to be uniform ($\eta = 4 \times 10^{-4}$; in dimensionless unit) in the whole region except the layer $k = 1$. All other setups during $59 < t \leq 71$ are the same as those before $t = 59$.

The third control simulation, referred to as “Simulation No-eruption” (abbreviated as “Simulation Ne”), is also composed of three phases: the shearing phase ($0 \leq t \leq 18$), the converging phase ($18 < t \leq 59$), and the relaxation phase ($59 < t \leq 72$). The setups in the three phases of “Simulation Ne” are the same as those in the three phases of “Simulation Ue,” respectively, except that the converging motion is switched off a little earlier, during $58 < t \leq 59$.

A.2. Kinematics of CME Progenitors/CMEs in Control Simulations

The kinematics of CME progenitors and CMEs in these three control simulations is estimated by a method same as that applied to “Simulation De.” For these three simulations, the point, from which the overlying field line is traced, is the same as that used in “Simulation De.” The velocity at this fixed point is extremely small, very close to or equal to zero, in all phases of all three simulations.

The kinematics of CME progenitors and CMEs in control simulations and “Simulation De” is shown in Figures A1(a)–(c). We note that, for three control simulations, the decreasing acceleration or even negative acceleration in a period shortly after switching off the driving motion (e.g., $59 \leq t < 61$ in “Simulation He,” $59 \leq t < 61$ in “Simulation Ue,” $58 \leq t < 62$ in “Simulation Ne”) could be due to the viscous and resistive effects, as well as the relative relaxations of magnetic tension and pressure around the tipping point of the equilibrium curve (Démoulin & Aulanier 2010).

A.3. Onset Time of Torus Instability

For all four simulations, in the period $57 \leq t \leq 64$, the flux rope is basically along the y -direction (Figure A2; taking examples at $t = 57$ and $t = 64$ in “Simulation De”). Therefore, the magnetic field at the intersection of the flux rope axis and the plane $y = 0$ is considered in the y -direction in this period,

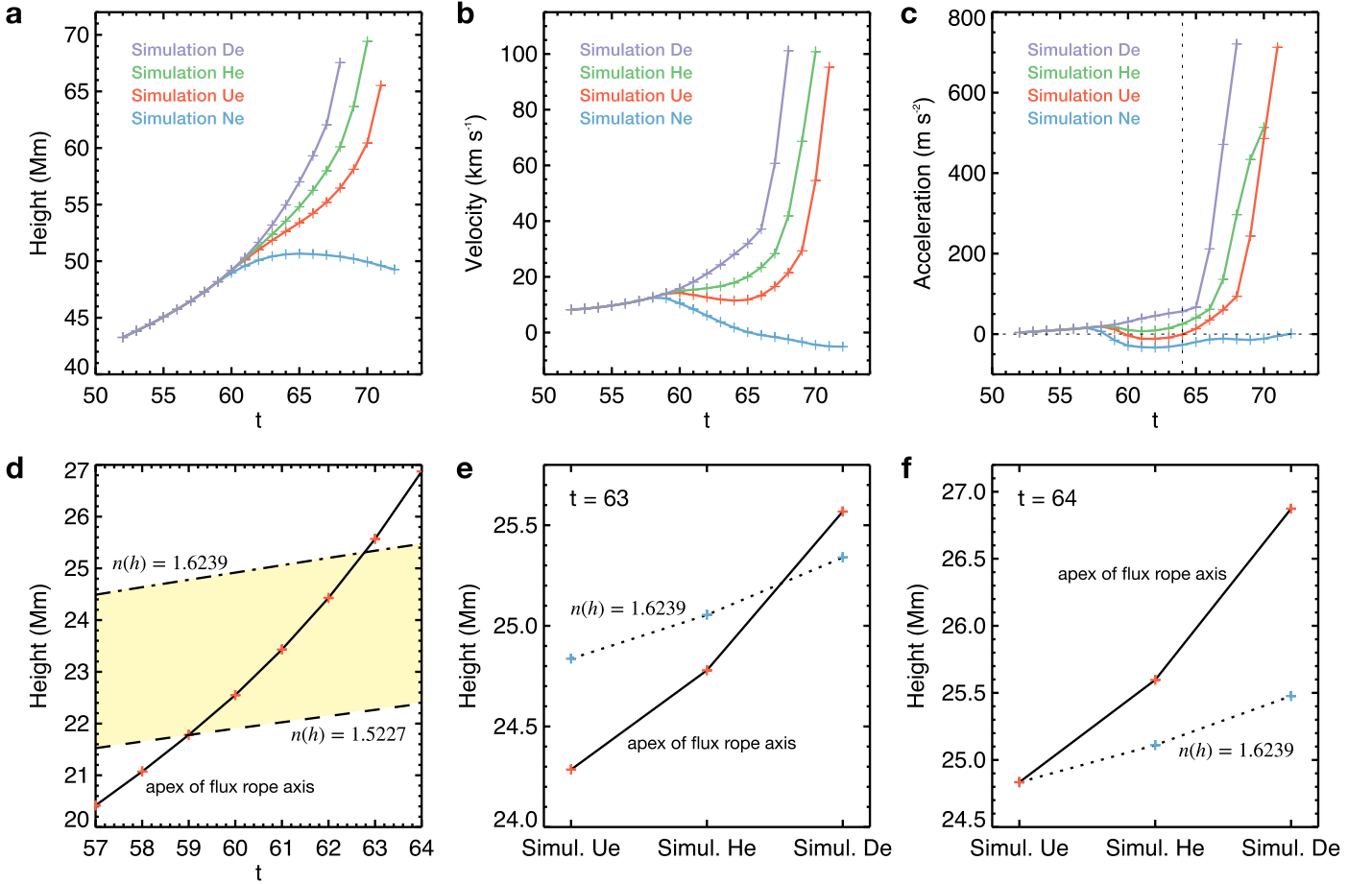


Figure A1. Kinematics of CME progenitors and CMEs in four simulations and estimation of the onset time of the torus instability in “Simulation De.” (a)–(c) Kinematics of CME progenitors and CMEs in “Simulation De” (purple curves), “Simulation He” (green curves), “Simulation Ue” (red curves), and “Simulation Ne” (blue curves). In panel (c), the vertical and horizontal black dashed lines mark that the flux rope acceleration in “Simulation Ue” is close to zero at $t = 64$. (d) The solid curve exhibits the height of the flux rope axis apex during $57 \leq t \leq 64$ in “Simulation De.” The dotted-dashed curve (long-dashed curve) represents the evolution of the height (h) during $57 \leq t \leq 64$ in “Simulation De,” the height which meets the condition that the decay index at $(0, 0, h)$ equals 1.6239 (1.5227) at each moment. The yellow region marks the range for the critical height of the torus instability onset during $57 \leq t \leq 64$ in “Simulation De.” (e) The solid curve shows the evolution of the height of the flux rope axis apex at $t = 63$, from “Simulation (abbreviated as Simul.) Ue” to “Simulation He” to “Simulation De.” The dashed curve shows the evolution of the height (h), which meets the condition that the decay index at $(0, 0, h)$ equals 1.6239 at $t = 63$, from “Simulation Ue” to “Simulation He” to “Simulation De.” (f) Same as panel (e) but for those at $t = 64$.

and the intersection is determined with the contour of $B_x = 0$ and the contour of $B_z = 0$ in the plane $y = 0$. The axis field line is then traced from the intersection. The decay index, $n = -d(\ln B_r)/d(\ln h)$, describes the decay rate of the component (B_r) of the potential field, which is transverse and perpendicular to the flux rope, with the height (h). At each analyzed moment, the potential field is extrapolated by the Green’s function method (performed by Solar Software (SSW; Freeland & Handy 2012) package code “optimization_fff.pro”) with B_z at the cell-center bottom surface as the input. During $57 \leq t \leq 64$, the component $B_r(h)$ is defined as the absolute value of B_x of the potential field at $(0, 0, h)$, considering the flux rope axis is along the y -direction, and the horizontal coordinate of its apex is around $(0, 0)$.

We first analyze the kinematic evolution in “Simulation Ue” (see red curves in Figures A1(a)–(c)). We consider that the onset time of the CME eruption in the physical sense (i.e., the time when the stable equilibrium of the flux rope is broken) is between $t = 59$ and $t = 64$ for the following two reasons: (a) The CME progenitor fails to erupt in “Simulation Ne,” in which all setups are the same as those in “Simulation Ue” but

the converging motion is switched off during $58 < t \leq 59$. This means that the CME in “Simulation Ue” erupts after $t = 58$. The earliest limit of its eruption onset time is therefore set at $t = 59$. (b) The acceleration in “Simulation Ue” changes from negative to positive at $t \sim 64$ and increases continuously after that (Figure A1(c)). This indicates that the flux rope is out of equilibrium after that, and thus the latest limit of the eruption onset time is set at $t = 64$. For “Simulation Ue,” the decay index of the potential field at the apex of the flux rope axis is 1.5227 at $t = 59$ and 1.6239 at $t = 64$, very close to the threshold of 1.5 for the occurrence of torus instability (Kliem & Török 2006), indicating that the CME eruption is highly probably triggered by the torus instability. The HFT reconnection that starts earlier ($t = 46$) is considered unable to lead to the eruption as the eruption fails in the presence of HFT in “Simulation Ne” (Aulanier et al. 2010).

Next, we analyze the kinematic evolution in “Simulation De.” We consider that the (pre-)eruptive flux rope in “Simulation De” is quite similar to that in “Simulation Ue” in the period $59 \leq t \leq 64$, as the height of the flux rope axis apex in “Simulation Ue” is only 7.6% lower than that in

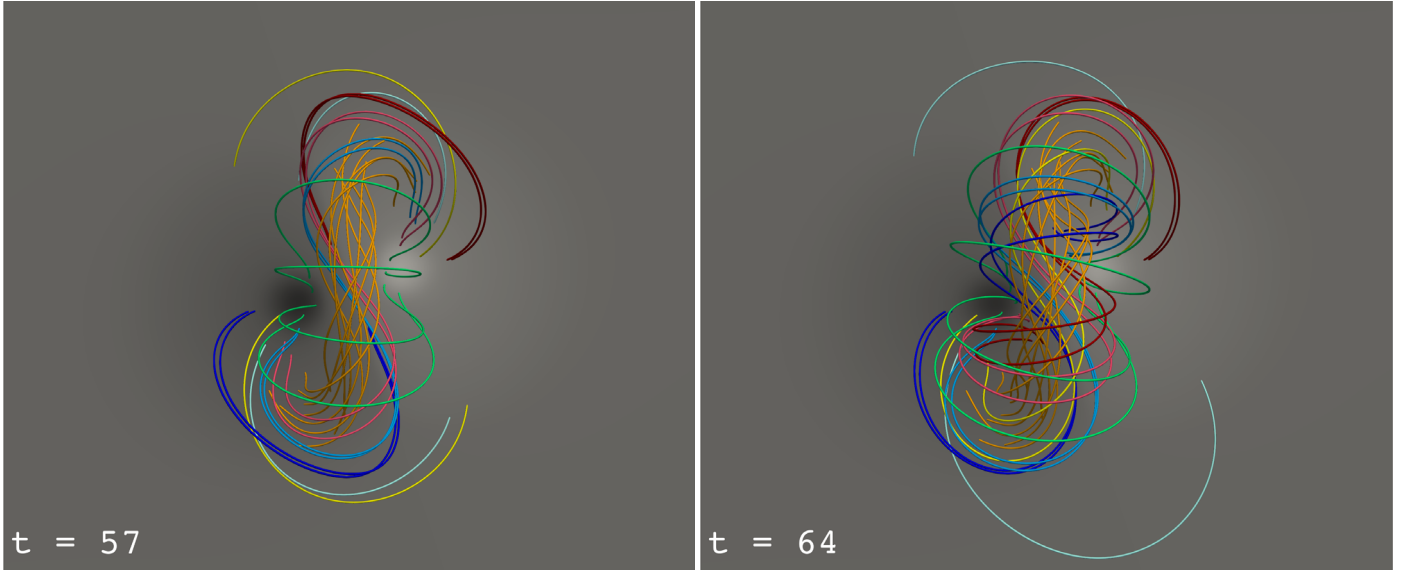


Figure A2. Top views of magnetic field lines in Figure 2(b). The left panel is at $t = 57$ and the right panel is at $t = 64$. The vertical direction is the y -direction.

“Simulation De” at $t = 64$. Therefore, if the torus instability also sets in “Simulation De,” the critical decay index for the torus instability onset should be in a range quite similar to $1.5227 \leq n \leq 1.6239$. In the following, we take the range $1.5227 \leq n \leq 1.6239$ for the critical decay index in “Simulation De.” In Figure A1(d), it is clear that the height of the flux rope axis apex in “Simulation De” is already higher than the height of the upper limit of the critical decay index at $t = 63$, indicating that the torus instability could set in “Simulation De” and that its onset time should be before $t = 63$. The earliest onset time of the torus instability in “Simulation De” is still $t = 59$, as the apex of the flux rope axis reaches the height of the lower limit of the critical decay index at this moment. Therefore, we summarize that the torus instability sets in “Simulation De” during $59 \leq t < 63$.

We note that it is not an accident that the time range of the torus instability onset in “Simulation De” is earlier than that in “Simulation Ue.” In the period $60 < t \leq 64$, the driving motion becomes stronger and stronger from “Simulation Ue” to “Simulation He” to “Simulation De,” with the maximum speed of the driving motion varying from 0 to 0.08 to 0.16 (in dimensionless unit). In Figures A1(e), (f), we show that, on the one hand, for these three simulations, the flux rope in the simulation with a stronger driving motion could rise to a higher altitude at the same moment (taking examples at $t = 63$ (see panel (e)) and at $t = 64$ (see panel (f))). On the other hand, in comparison among the three simulations, the one with a stronger driving motion has a higher height corresponding to the same critical decay index at the same moment (see panels (e) and (f)). However, it is clear that such a difference in the height of the flux rope axis is much larger than the difference in the height of a certain decay index, when comparing each two of these three simulations. This suggests that in comparison among different simulations, the stronger the imposed driving motion the earlier the flux rope axis reaches the height of the critical decay index, and thus the earlier the torus instability starts, regardless of the change in the critical decay index itself.

Appendix B Flux Rope Boundary

The flux rope boundary and the reconnection region are identified with the squashing degree Q which measures the mapping of the field lines. The squashing degree Q (Titov et al. 2002) is derived by:

$$Q = \frac{\left(\frac{\partial X}{\partial x}\right)^2 + \left(\frac{\partial X}{\partial y}\right)^2 + \left(\frac{\partial Y}{\partial x}\right)^2 + \left(\frac{\partial Y}{\partial y}\right)^2}{\left| \frac{\partial X}{\partial x} \frac{\partial Y}{\partial y} - \frac{\partial X}{\partial y} \frac{\partial Y}{\partial x} \right|} \quad (\text{B1})$$

with the code FastQSL (Zhang et al. 2022), where (x, y) and (X, Y) are coordinates of two footpoints of a field line.

The QSLs refer to the locations where $\log Q$ is much larger than 2 (Titov et al. 2002), and here we define the QSLs as the region where $\log Q \geq 3$. In the following, we take the flux rope at $t = 58$ in “Simulation De” as an example to explain how we determine the flux rope boundary. In the plane $y = 0$, the bottom and side boundaries of the flux rope can be exactly determined by the QSLs, while the top boundary is blurred as the QSLs are not closed there (Figure B1). We determine the top boundary qualitatively at the top edge of the strong downward Lorentz force region, i.e., the apex of the flux rope is roughly at $z = 3.3$ (in the dimensionless unit; see Figure 6(a)). This determination is reasonable for the following reasons. First, as shown in Figure B1, the weakly twisted field lines traced from the downward Lorentz force region (yellow field lines) are mostly anchored in the regions partially surrounded by the QSL footprints. They compose a flux rope configuration together with the highly twisted field lines traced from the upward Lorentz force region (green field lines). Second, the tops of the high mass density region (represented by the gravity in Figure 6(c)) and of the high current density region (represented by the ohmic heating rate in Figure 11) are also around $z = 3.3$ in the plane $y = 0$, also indicating that the flux rope apex is around $z = 3.3$.

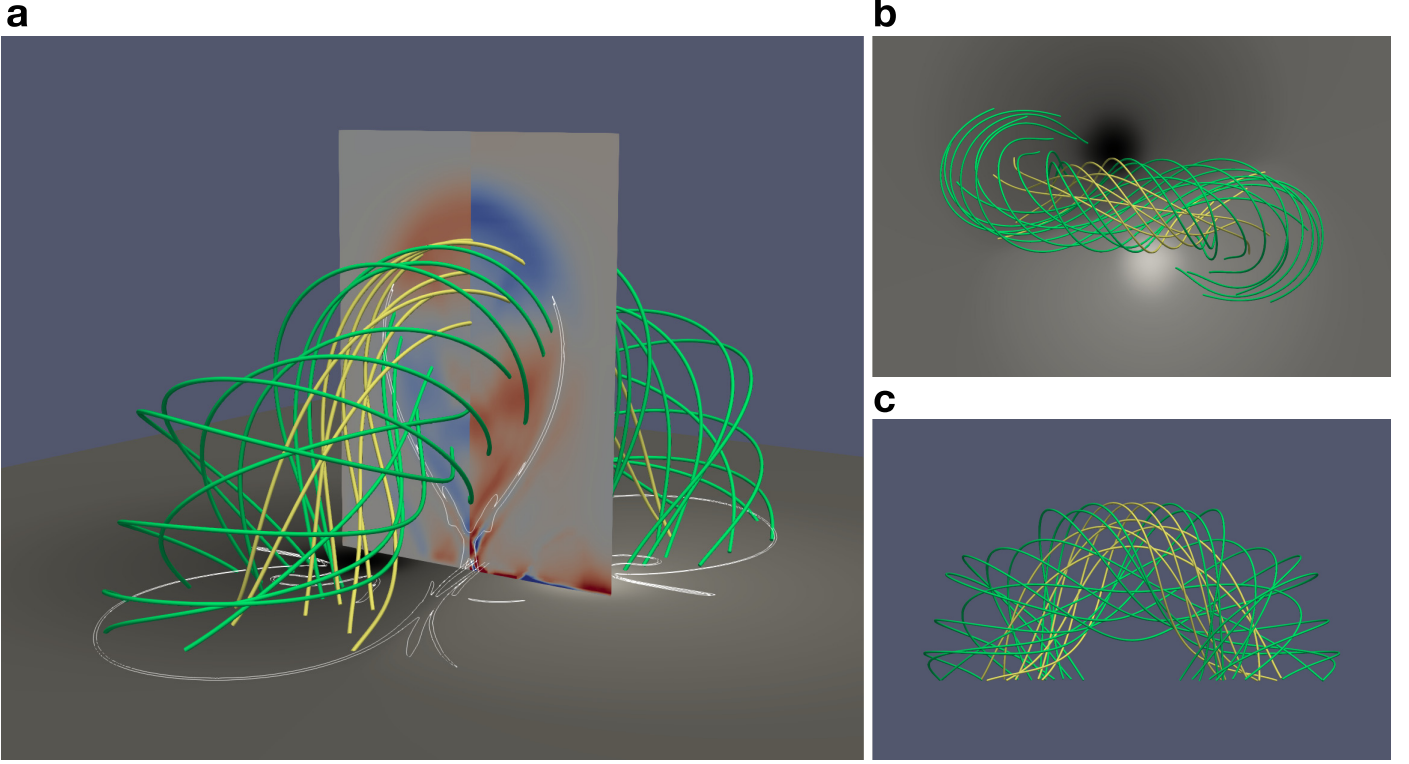


Figure B1. Magnetic field lines in the flux rope at $t = 58$. (a) Forces on the plane $y = 0$ and field lines in the flux rope. The green (yellow) shows the highly (weakly) twisted field lines. In the plane $y = 0$, the left half panel shows the z -component of the thermal pressure gradient force, and the right half panel shows the z -component of the Lorentz force. The colors and the scales of the forces are the same as those in Figure 6. The cell-center bottom surface shows the distribution of B_z . The white contours on the bottom surface and the vertical plane represent the contours of QSLs. (b) Top view of panel (a). (c) Face-on view of panel (a).

Appendix C Estimating the Reconnection Electric Field

We estimate the reconnection electric field with a method commonly used in observations (Qiu et al. 2002). In brief, the reconnection electric field (E) is derived by $E = v_Q B_z$, where v_Q is the separation speed of the QSL footprint in the direction perpendicular to the PIL and B_z is the z -component of the magnetic field at the QSL footprint. This estimation method is based on a 2D flare model but is considered still applicable to a 3D situation (Forbes & Lin 2000). We refer readers to the previous paper (Qiu et al. 2002) for more details of this method.

In Figures 8(a)–(e), we show the separation motion of the QSL footprint on the cell-center bottom surface. To estimate the separation motion speed, we set a slit (represented by the orange dashed lines in Figures 8(a)–(c)) on this surface, starting from the origin and along the direction perpendicular to the PIL. The time-slice plot of the normalized $\log Q$ (Figure 8(f)), where the $\log Q$ on the slit is normalized by its maximum at each moment, exhibits how the QSL footprint separates from the PIL. The center of the QSL footprint, where the normalized $\log Q$ reaches its local maximum, is marked by the red symbol at each moment. The phenomenon that the QSL footprint stays on the PIL before and at $t = 45$ confirms that the magnetic topology of the reconnection region is a BP in this period. The separation of the QSL footprint starts at $t = 46$, marking the first appearance of HFT at this moment. The separation speed (v_Q) is derived to be the derivative of the distance from the origin to the QSL footprint with time. Finally, the electric field of the HFT reconnection is derived by multiplying the separation speed with the local B_z . The electric field during

$46 \leq t \leq 51$ (see Figures 8(g), (h)) is represented by that derived from the orange slit, considering the reconnection still occurs in BP rather than HFT in many other places in this period. The electric field during $52 \leq t \leq 68$ (also see Figures 8(g), (h)) is represented by the average of the electric fields derived from the orange slit and three other slits (represented by the pink dashed lines in Figures 8(a)–(c); all of them crossing through HFT footprints rather than BP footprints since $t = 52$). The aim of the multiple measurements and averaging is to better show the evolution of the electric field in the entire HFT.

Appendix D Synthetic EUV Images of the CME Progenitor





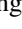
We synthesize the EUV images at the AIA 335 Å as observed from three side views by integrating the emissivity along each direction under the optically thin emission assumption. The passband is selected at 335 Å to best demonstrate the structure of the hot CME progenitor. The emissivity is derived from the temperature and the number density of electrons (which are dimensionalized with the dimensionless units; the number density is derived under the assumption of a fully ionized ideal gas with a hydrogen-helium abundance ratio of 10:1) with the AIA response function (performed by SSW package code “aia_get_response.pro”), and the integration is performed in a box where $-3.2 \leq x \leq 3.2$, $-4.9 \leq y \leq 4.9$, and $0.015 \leq z \leq 3.86$ (in dimensionless unit). To better show the flux rope structure, we show the percentage difference intensity rather than the

original synthetic intensity, which is derived by:

$$D_i = \frac{I_i - I_0}{I_0}, \quad (\text{D1})$$

where D_i and I_i are the percentage difference intensity and the original synthetic intensity at $t = t_i$, respectively, and I_0 is the original synthetic intensity at $t = 0$. We note that the percentage difference intensity in the flux rope, although sometimes negative, is still larger than that of its surroundings, clearly showing the presence of the hot CME progenitor.

ORCID iDs

Chen Xing  <https://orcid.org/0000-0002-6550-1522>
 Guillaume Aulanier  <https://orcid.org/0000-0001-5810-1566>
 Xin Cheng  <https://orcid.org/0000-0003-2837-7136>
 Chun Xia  <https://orcid.org/0000-0002-7153-4304>
 Mingde Ding  <https://orcid.org/0000-0002-4978-4972>

References

- Antiochos, S. K., DeVore, C. R., & Klimchuk, J. A. 1999, *ApJ*, **510**, 485
 Aulanier, G. 2014, in IAU Symp. 300, Nature of Prominences and their Role in Space Weather, ed. B. Schmieder, J.-M. Malherbe, & S. T. Wu (Cambridge: Cambridge Univ. Press), 184
 Aulanier, G. 2021, *NatAs*, **5**, 1096
 Aulanier, G., Démoulin, P., & Grappin, R. 2005, *A&A*, **430**, 1067
 Aulanier, G., Török, T., Démoulin, P., et al. 2010, *ApJ*, **708**, 314
 Chen, P. F. 2011, *LRSP*, **8**, 1
 Cheng, X., Ding, M. D., Zhang, J., et al. 2014, *ApJ*, **789**, 93
 Cheng, X., Guo, Y., & Ding, M. 2017, *ScChD*, **60**, 1383
 Cheng, X., Xing, C., Aulanier, G., et al. 2023, *ApJL*, **954**, L47
 Cheng, X., Zhang, J., Kliem, B., et al. 2020, *ApJ*, **894**, 85
 Cheng, X., Zhang, J., Saar, S. H., et al. 2012, *ApJ*, **761**, 62
 Dedner, A., Kemm, F., Kröner, D., et al. 2002, *JCP*, **175**, 645
 Démoulin, P., & Aulanier, G. 2010, *ApJ*, **718**, 1388
 Elovaara, J. 2007, Research Towards Applications in Europe II European Week (ESWW2), Vol. 344 (Dordrecht: Springer), 311
 Forbes, T. G., & Lin, J. 2000, *JASTP*, **62**, 1499
 Forbes, T. G., & Priest, E. R. 1984, *SoPh*, **94**, 315
 Freeland, S. L., & Handy, B. N., 2012 SolarSoft: Programming and data analysis environment for solar physics, Astrophysics Source Code Library, ascl:1208.013
 Gosling, J. T. 1993, *JGR*, **98**, 18937
 Green, L. M., & Kliem, B. 2009, *ApJL*, **700**, L83
 Green, L. M., Török, T., Vršnak, B., et al. 2018, *SSRv*, **214**, 46
 Harten, A., Lax, P., & van Leer, B. 1983, *SIAMR*, **25**, 35
 Janvier, M., Aulanier, G., Bommier, V., et al. 2014, *ApJ*, **788**, 60
 Jiang, C., Feng, X., Liu, R., et al. 2021, *NatAs*, **5**, 1126
 Kahler, S. W., Moore, R. L., Kane, S. R., et al. 1988, *ApJ*, **328**, 824
 Kaithakkal, A. J., & Solanki, S. K. 2019, *A&A*, **622**, A200
 Khodachenko, M. L., Ribas, I., Lammer, H., et al. 2007, *AsBio*, **7**, 167
 Kliem, B., & Török, T. 2006, *PhRvL*, **96**, 255002
 Lemen, J. R., Title, A. M., Akin, D. J., et al. 2012, *SoPh*, **275**, 17
 Lin, J., & Forbes, T. G. 2000, *JGR*, **105**, 2375
 Masson, S., Antiochos, S. K., & DeVore, C. R. 2019, *ApJ*, **884**, 143
 Moore, R. L., Sterling, A. C., Hudson, H. S., et al. 2001, *ApJ*, **552**, 833
 Patsourakos, S., Vourlidas, A., & Stenborg, G. 2013, *ApJ*, **764**, 125
 Prasad, A., Kumar, S., Sterling, A. C., et al. 2023, *A&A*, **677**, A43
 Priest, E. R., & Démoulin, P. 1995, *JGR*, **100**, 23443
 Qiu, J., Lee, J., Gary, D. E., et al. 2002, *ApJ*, **565**, 1335
 Savcheva, A. S., van Ballegoijen, A. A., & DeLuca, E. E. 2012, *ApJ*, **744**, 78
 Schrijver, C. J., Aulanier, G., Title, A. M., et al. 2011, *ApJ*, **738**, 167
 Schrijver, C. J., Elmore, C., Kliem, B., et al. 2008, *ApJ*, **674**, 586
 Simnett, G. M., & Harrison, R. A. 1985, *SoPh*, **99**, 291
 Sterling, A. C., Moore, R. L., Berger, T. E., et al. 2007, *PASJ*, **59**, S823
 Suresh, A., & Huynh, H. T. 1997, *JCoPh*, **136**, 83
 Tanaka, T. 1994, *JCoPh*, **111**, 381
 Titov, V. S., Hornig, G., & Démoulin, P. 2002, *JGRA*, **107**, 1164
 Titov, V. S., Priest, E. R., & Démoulin, P. 1993, *A&A*, **276**, 564
 Xia, C., Chen, P. F., & Keppens, R. 2012, *ApJL*, **748**, L26
 Xia, C., Teunissen, J., El Mellah, I., et al. 2018, *ApJS*, **234**, 30
 Xing, C., Li, H. C., Jiang, B., et al. 2018, *ApJL*, **857**, L14
 Yang, G., Xu, Y., Cao, W., et al. 2004, *ApJL*, **617**, L151
 Zhang, J., Cheng, X., & Ding, M.-D. 2012, *NatCo*, **3**, 747
 Zhang, J., & Dere, K. P. 2006, *ApJ*, **649**, 1100
 Zhang, J., Dere, K. P., Howard, R. A., et al. 2001, *ApJ*, **559**, 452
 Zhang, P., Chen, J., Liu, R., et al. 2022, *ApJ*, **937**, 26
 Zhao, J., Gilchrist, S. A., Aulanier, G., et al. 2016, *ApJ*, **823**, 62
 Zou, P., Jiang, C., Wei, F., et al. 2019, *ApJ*, **884**, 157
 Zuccarello, F. P., Aulanier, G., & Gilchrist, S. A. 2015, *ApJ*, **814**, 126